1 **The Morphology of Ice and Liquid Brine in the Environmental SEM: A**
2 **Study of the Freezing Methods**

3

4 Ľubica Vetráková,[1] Vilém Neděla,[1] Jiří Runštuk,[1] Dominik Heger[2]

5 [1]Environmental Electron Microscopy Group, Institute of Scientific Instruments of the Czech Academy
6 of Sciences, Brno, Czech Republic

7 [2]Department of Chemistry, Faculty of Science, Masaryk University, Brno, Czech Republic

8 Correspondence to: Ľubica Vetráková (vetrakova@isibrno.cz), Dominik Heger
9 (hegerd@chemi.muni.cz)

10

Abstract

12 The microstructure of polycrystalline ice with a threading solution of brine controls its numerous
13 characteristics, including the ice mechanical properties, ice-atmosphere interactions, sea-ice albedo,
14 and (photo)chemical behavior in/on the ice. Ice samples were previously prepared in laboratories to
15 study various facets of ice-impurities interactions and (photo)reactions to model natural ice-impurities
16 behavior. We examine the impact of the freezing conditions and solute (CsCl used as a proxy for
17 naturally occurring salts) concentrations on the microscopic structure of ice samples via an
18 environmental scanning electron microscope. The method allows us to observe in detail the ice
19 surfaces, namely, the free ice, brine puddles, brine-containing grain boundary grooves, individual ice
20 crystals, and imprints left by entrapped air bubbles at temperatures higher than -25°C. The amount of
21 brine on the external surface is found proportional to the solute concentration and is strongly
22 dependent on the sample preparation method. Time-lapse images in the condition of slight
23 sublimation reveal sub-surface association of air bubbles with brine. With rising temperature (up to −
24 14 °C), the brine surface coverage increases to remain enhanced during the subsequent cooling and
25 until the final crystallization below the eutectic temperature. The ice recrystallization dynamics
26 identifies the role of surface spikes in retarding the ice boundaries propagation (Zeener pining). The
27 findings thus quantify the amounts of brine exposed to incoming radiation, available for the gas
28 exchange, and influencing other mechanical and optical properties of ice. The results have
29 straightforward implications for artificially prepared and naturally occurring salty ices.

30

31 ## 1 Introduction

32

33 Ice and snow are important reaction media in which chemical compounds (impurities) can be
34 accumulated, transformed, and released back to the environment (Bartels-Rausch et al., 2014). The
35 location of impurities within a frozen sample and its time evolution are crucial in multiple respects:
36 they determine the mechanical and optical properties of the material and thus must be considered in
37 relation to snowpack stability, avalanches, sea ice mechanics, and climate change research (Blackford
38 et al., 2007;Hobbs, 2010;Dash et al., 2006;Wåhlin et al., 2014). The location of impurities most
39 probably influences the compounds' reactivity as their availability to incoming light radiation and/or
40 gaseous reactants substantially differs depending on whether the impurities are located on the ice
41 surface or buried in the frozen bulk (Hullar and Anastasio, 2016). However, the information combining
42 the reactivity of compounds with their locations is essentially missing. Impurities are usually not

incorporated into the ice lattice (Krausková et al., 2016;Hobbs, 2010;Wilson and Haymet, 2008). As ice is highly intolerant to impurities, these are segregated to an unfrozen freeze-concentrated solution (FCS) during the growth of ice crystals. The FCS can be located in the veins between the ice crystals, (micro)pockets within the ice structure, or puddles and grain boundary grooves on the ice surface. When the mixture is cooled below the eutectic temperature (T_{eu}), the FCS may crystallize or vitrify (Salnikova et al., 2015;Bogdan et al., 2014).

To determine the actual positions of chemical compounds in ice samples, various microscopic techniques are used, including optical (Bogdan et al., 2014;Bogdan and Molina, 2017), fluorescence (Cheng et al., 2010;Roessl et al., 2015), electron (Blackford et al., 2007;Chen and Baker, 2010;Rosenthal et al., 2007;Barnes et al., 2002), and confocal Raman (Dong et al., 2009) microscopies. While optical microscopy can be applied at environmentally relevant temperatures and pressures, very low pressure conditions (10^{-4} to 10^{-2} Pa) are needed in the specimen chamber of a conventional scanning electron microscope (SEM). At such low pressures, ice sublimes very rapidly due to its high vapor pressure (Blackford, 2007); for that reason, ice samples are observable only at very low temperatures (below −120 °C) in a SEM. (Blackford et al., 2007) These conditions are far from naturally relevant ones. Conversely, however, electron microscopy resolves fine structures two orders of magnitude smaller compared to those examined with optical microscopy, and its depth of field is much larger. Moreover, the ice surface appears opaque in a SEM, and its surface topography is thus defined significantly better than possible using optical microscopy (Blackford, 2007). In order for electron microscopy to be usable at higher pressures, the environmental scanning electron microscope (ESEM) was designed (Danilatos, 1993). The ESEM can operate at specimen chamber pressures of up to thousands of Pascals, and such capability allows frozen samples to be inspected at higher temperatures, even up to the samples' melting point. To prevent ice sublimation, water vapor can be purged into the specimen chamber; thus, the imaging is performed under closer-to-natural conditions. Further, ionization of the gas in the specimen chamber of the ESEM prevents the sample from being charged, rendering the technique very convenient for imaging electrically non-conductive samples without the need of conductive coating. The ESEM is therefore becoming increasingly popular within research into pure ice (Nair et al., 2018;Magee et al., 2014;Chen et al., 2017) and ice-impurities interactions under static and dynamically changing conditions (Krausko et al., 2014;Yang et al., 2017). While electron microscopy visualizes the sample surface in detail, micro-computed tomography was recently applied to investigate solute locations in the frozen bulk (Hullar and Anastasio, 2016). Using this technique, the authors were able to visualize the locations of solutes (CsCl or rose bengal), gas, and ice in 3D.

Salt solutions are abundant in the natural environment; seawater alone represents 96.5% of water on the Earth (Gleick, 1993). In wintertime, sea ice covers an area of up to 7% of the Earth's surface and, as such, embodies one of the largest biomes (Thomas, 2017). Salts and ice also coexist in sea aerosols (Knipping et al., 2000;Zobrist et al., 2008), coastal regions, on frost flowers (Douglas et al., 2012), and also in ice cores (Ohno et al., 2006, 2005;Vega et al., 2018).

Well-conceived laboratory investigation of the ice-impurity interaction has the potential to simplify complex natural systems. Laboratory-based studies of the (photo)chemical reactions of frozen aqueous solutions have improved the understanding of the (photo)chemistry occurring in cold environments (Bartels-Rausch et al., 2014;Klanova et al., 2003). However, the dissonance between results from individual laboratories as regards the photodegradation rates (Kahan et al., 2010;Ram and Anastasio, 2009) points to the fact that there still remain key factors influencing the reactivity in a frozen solution which were not comprehended previously.

The impurities' locations were most often deduced from the sample preparation methods; for example, freezing an aqueous solution involved the precondition of placing the impurities inside the ice matrix. Subsequent breaking of the ice into small pieces was proposed to bring the impurities on

90 the ice surface (Kahan et al., 2010); this assumption was recently questioned (Hullar et al., 2018). Other
91 studies suggested that freezing an aqueous solution places the impurities prevalently inside the ice
92 interior, whereas deposition of the organics from the vapour phase accommodates them on the ice
93 surface (Ondrušková et al., 2018;Vetráková et al., 2017;Krausko et al., 2015b;Krausko et al.,
94 2015a;Kania et al., 2014;Heger et al., 2011;Hullar et al., 2018). Conversely, nebulizing the solution into
95 liquid nitrogen was assumed to produce ice spheres with the organic impurities on their surfaces
96 (Kurkova et al., 2011).
97   To establish a direct proof of salt location in frozen samples, we herein applied various methods
98 to freeze caesium chloride (CsCl) solutions. We intended to determine how the ice impurities' location
99 and surface availability are affected by the freezing technique, temperature, and salt concentrations.
100 The ESEM technology was utilized for the visualization due to its ability to represent the samples'
101 surface topography together with the impurities' locations. CsCl was chosen as the model salt, being
102 similar to NaCl and providing very good microscopic contrast; thus, the presence of brine on the
103 surface of the frozen samples can be clearly monitored, and the location of sea water brine on sea ice
104 can be inferred.
105

106 2 Methods

107 The microscopic images were recorded using an AQUASEM II, a Tescan VEGA SEM modified at the
108 Institute of Scientific Instruments of the Czech Academy of Sciences (Tihlarikova et al., 2013;Nedela,
109 2007). This ESEM is capable of imaging wet, electrically non-conducting samples at chamber pressures
110 as high as 2,000 Pa and temperatures of down to −27 °C. The advantages of the AQUASEM II in the
111 imaging of frozen samples had been described previously (Krausko et al., 2014;Yang et al., 2017).

112 2.1 Preparation of the samples

113 CsCl solutions with the concentrations of 0.005, 0.05, and 0.5 M were prepared by dissolving an
114 appropriate amount of CsCl in MilliQ H_2O. The molar concentrations correspond to molalities of 0.005,
115 0.050, and 0.512 mol/kg, respectively, using the solution densities at 20 °C from Reiser et al. (2014);
116 the position of these concentrations can be realized on the phase diagram for the CsCl-water (Figure
117 1) (Gao et al., 2017). Prior to the measurement, the solutions had been filtered through a 0.45 μm filter
118 to exclude impurities that might interfere with the microscopic observations. The solutions were
119 frozen at atmospheric pressure via four distinct methods:

(I)   Spontaneous freezing of a droplet without seeding. A droplet was put onto the silicon sample
120   holder of the ESEM at room temperature (about 23 °C). The temperature of the sample holder,
121   controlled by a Peltier stage, was lowered gradually (the cooling rate corresponded to
122   approximately 0.5 °C/s) until the sample froze spontaneously. The nucleation temperature
123   ranged from −16 to −18 °C in the replicate experiments. After becoming frozen, the sample
124   was cooled down to the initial observation temperature of −22 to −25 °C.
126 (II)   Freezing of a droplet with seeding. A droplet was placed onto the sample holder of the ESEM,
127   and its temperature was set to −2 °C; then, after thermal equilibration, several small ice
128   crystals were added to the edge of the sample to initiate the nucleation process. Subsequently,
129   the temperature of the sample holder was lowered down to the initial observation value.
130 (III) Spraying into a vessel containing liquid nitrogen (LN). Small ice spheres (similar to artificial
131   snow) were formed and then transferred onto the microscope sample holder precooled to
132   −25 °C.
133 (IV)   Fragmentation of an LN-frozen sample. The applied CsCl solution enclosed in a hard gelatine
134   capsule (approx. length of 25 mm, diameter of 8 mm) was immersed in LN. After freezing, the
135   sample was fragmentized with a scalpel; thus, irregularly shaped pieces were formed, and the

3

136   former interior of the sample was revealed. The fragments from the interior of the sample
137   were transferred onto the ESEM sample holder precooled to −25 °C.

138   To deliver the samples undisturbed for the microscopic observation, a thin layer of ice from condensed
139   moisture was intentionally created on their surfaces in all of the preparation methods. This layer
140   protected the samples from sublimating during the pump-down of the specimen chamber. After its
141   sublimation at the beginning of the imaging, the original surface was revealed in each of the samples.
142
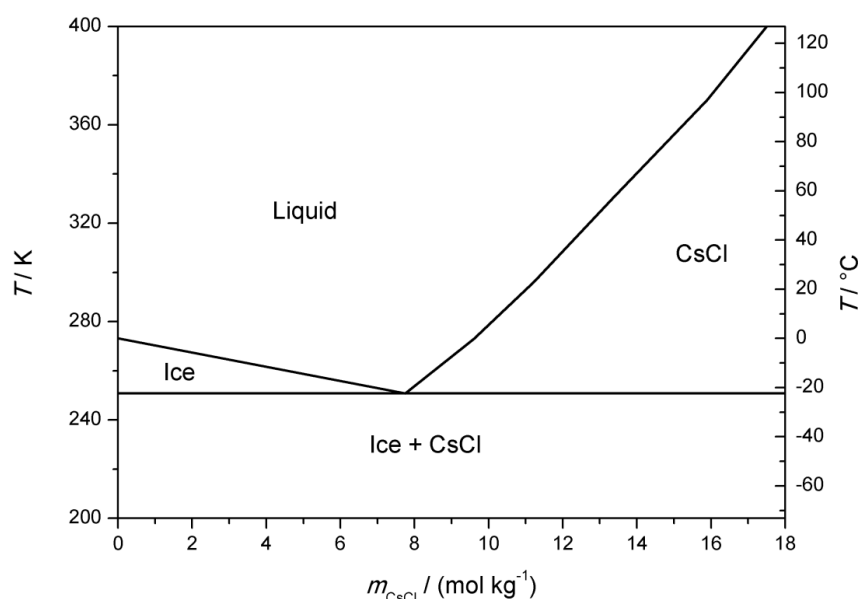
Figure 1. The phase diagram for CsCl-water. Adopted from Gao et al. (2017).

2.2 Imaging in the ESEM

147   The electron beam energy of 20 keV and a YAG:Ce^{3+} scintillation backscattered electrons (BSE)
148   detector, sensitive to the region encompassing the top 1,500 nm, were employed for the imaging. In a
149   number of instances, the samples were imaged with an ionization detector of secondary electrons,
150   recording mainly signals from the thin subsurface layer (up to 5 nm); the device enabled us to obtain
151   information about the topology of the surface (Neděla et al., 2015). In all of the measurements, a low
152   beam current (40 pA) and a short dwell time (14 µs) were employed to minimize radiation damage to
153   the frozen samples. During the experiments, we maintained the nitrogen gas partial pressure of 500
154   Pa inside the specimen chamber. Besides the nitrogen gas, water vapor was also purged into the
155   chamber; the relative humidity was kept slightly below the sublimation curve values to prevent
156   moisture condensation on the ice surface. Somewhat slow ice sublimation was observed as conditions
157   exactly matching the sublimation curve are difficult to establish inside the specimen chamber of the
158   ESEM. For a fresh sample, the initial temperature of the sample holder was usually set to −25 °C
159   (occasionally being −22 or −23.5 °C). Then, the temperature was gradually changed, and its impact on
160   the brine abundance on the surface of the sample was monitored; however, the temperature of the
161   sample surface might differ from that of the sample holder. Heating the sample surface by an electron

162 beam and the relatively warm gas inside the specimen chamber, together with the subsequent cooling
163 due to ice sublimation and/or water evaporation from the brine, affects the surface temperature. We
164 estimate that the surface of a frozen sample is up to 2 °C warmer compared to that of the sample
165 holder; this estimation is based on the difference between the published T_{eu} of the CsCl-water mixture,
166 ranging from −24.83 to −22.3 °C (Cohen-Adad, 1991;Dubois et al., 1993;Fujiwara and Nishimoto,
167 1998;Monnin and Dubois, 1999;Chen et al., 2005;Gao et al., 2017), and the holder temperature at
168 which the brine starts to crystallize. In our case, the value corresponded to approximately −25 °C.
169

2.3 Estimating the brine surface coverage

171 We used a BSE detector having high sensitivity to atoms with large atomic numbers; thus, in the ESEM
172 images, the sample surface covered with CsCl is white, while the grey areas represent the ice. To
173 estimate the extent of the sample surface covered with the brine, Mountains® Software (Digital Surf)
174 was applied. For each image, areas with brightness above the chosen threshold were selected in the
175 software to best visually represent the brine-covered regions (Figure S1), and their relative surface
176 occurrence was determined. A constant threshold could not be employed for all of the images due to
177 the fact that, during the actual image acquisition, the parameters of the detector (and thus the
178 brightness and contrast of the image) were often changed based on the intensity of the detected signal
179 to avoid under- or overexposure. If the signal is locally too intensive (e.g., there are spots with a large
180 amount of the brine), the detector sensitivity must be lowered during the image acquisition to prevent
181 oversaturation; thus, spots with a low amount of the brine might not be visible in the image, and the
182 surface coverage could be underestimated. Conversely, with the CsCl signal too low the brightness of
183 the brine might be comparable to that of the surface irregularities (as the detector is also sensitive to
184 the morphology of the sample, albeit to a limited extent only), leading to them being misinterpreted
185 as small brine-containing spots. Such a situation would then cause overestimated brine surface
186 coverage. The estimated coverage can therefore be directly compared exclusively in samples with
187 similar amounts of the salt (similar concentration), where the detector response differences are
188 negligible.
189

3   Results and discussion

191

192 Representative examples of the non-seeded samples, seeded samples, and ice spheres of three CsCl
193 concentrations (0.5 M, 0.05 M, and 0.005 M) are displayed in Figure 2. These images were recorded at
194 the very beginning of the microscopic observations and are thus very little affected by the sublimation
195 and specific conditions inside the specimen chamber of the ESEM (e.g., low pressure and possible
196 interactions with the electron beam). When BSEs are detected, merely the material contrast is
197 revealed in most cases. The white areas in the images represent the CsCl-containing brine or CsCl
198 crystals, while the dark or grey regions indicate the ice. Certain limited topographical information is
199 also obtained; it is visualized via various shades of grey. We measured >50 samples and analyzed the
200 acquired micrographs; from these, we then evaluated the impact of the freezing method and the salt
201 concentration on the appearance of the surfaces of the frozen samples, location of the brine, and sizes
202 of the ice crystals and grain boundary grooves.
203
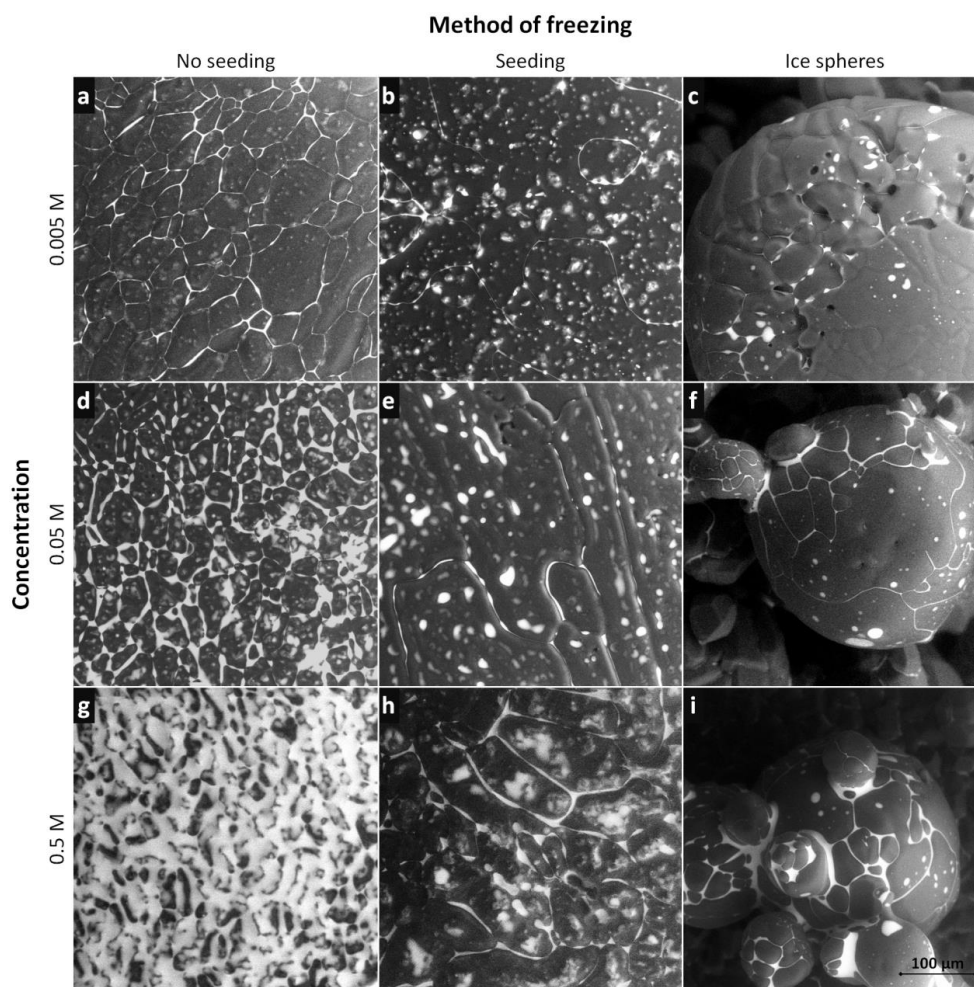
Figure 2. The ESEM images of the frozen samples prepared from the 0.005, 0.05, and 0.5 M CsCl solutions via the spontaneous freezing of a supercooled (non-seeded) droplet (a, d, g); freezing a droplet seeded with ice crystals (b, e, h); and spraying the solution into LN (c, f, i). The images were acquired at the very beginning of the observations, at the following temperatures: −22 °C (f, h, i); −23.5 °C (a-c); and −25 °C (d, e, g). The grey areas represent the ice, and the white regions denote the CsCl brine. Images of two additional samples for each freezing method and concentration are provided in SI (Figures S7-S15).

3.1 Appearance of the surface of the frozen samples

3.1.1 Non-seeded samples (Figure 2, left column). The brine was located mainly at the grain boundary grooves. For the CsCl concentration of 0.005 M, the grooves were well visible; no brine puddles were located on the sample surface. As the concentration was increased to 0.05 M, the grain boundary grooves became thicker, and small brine puddles appeared on the surface. The surfaces of the samples (0.005 M and 0.05 M) were not smooth, with visible small humps. The surface of the most concentrated sample (0.5 M) was almost completely covered with a brine layer already at the beginning of the observations; during the procedure, the surface became completely brine-flooded. Thus, the ice grains and grain boundary grooves could not be sufficiently recognized in this case.

6

220 **3.1.2 Seeded samples** (Figure 2, middle column). The amount of CsCl at the grain boundaries was
221 apparently much smaller compared to that in the non-seeded samples: the grain boundaries were
222 barely visible in the microscopic images of the 0.005 and 0.05 M seeded samples, and the surface of
223 the 0.5 M seeded sample was not brine-flooded. However, brine puddles were abundant on the
224 surfaces of the seeded samples. The surfaces were not smooth, with numerous humps formed (vide
225 infra).
226 **3.1.3 Ice spheres** (Figure 2, right column). Spraying the solution into LN led to the formation of ice
227 spheres with typical diameters ranging between 100 and 300 μm. Their prevalently regular and
228 spherical shapes indicate that the droplets froze during levitation above the LN surface due to the
229 inverse Leidenfrost effect: if they had frozen inside the LN volume, the shapes would have been pear-
230 like (Adda-Bedia et al., 2016). The surfaces of the spheres were smooth, lacking visible humps and
231 almost without brine puddles. For the concentration of 0.005 M, the grain boundaries were nearly
232 invisible, exhibiting very little brine on the sphere surfaces. As regards the CsCl concentrations of 0.05
233 M and 0.5 M, the brine was freeze-concentrated in the grain boundary grooves and at joints between
234 neighboring spheres.

235 ## 3.2 Sizes of the ice crystals

236 The average size of the ice crystals on the surfaces of the frozen samples depended on both the
237 freezing method and the solution concentration (Table 1). The largest ice crystals were detected in the
238 seeded droplet (the average sizes of 105, 91, and 48 μm for 0.005, 0.05, and 0.5 M CsCl, respectively).
239 These crystals exhibited oblong shapes, and therefore their longer and shorter dimensions were
240 evaluated separately; the average dimensions determined are listed in Table 1. As the larger crystals
241 often exceeded the field of view of the ESEM (see Figure S2, distance F), the calculated sizes are biased
242 towards lower values; thus, the average sizes should be somewhat larger. The smallest ice crystals
243 were formed in the supercooled non-seeded droplet; the average sizes equalled 44, 33, and 26 μm for
244 0.005, 0.5, and 0.5 M CsCl, respectively. Medium ice crystals (the average sizes of 50, 55, and 39 μm
245 for 0.005, 0.5, and 0.5 M CsCl, respectively) were observed on the surfaces of the ice spheres.
246

Concentration of CsCl / M	Average diameter of the ice crystals / μm				
	Non-seeded droplets	Seeded droplets			Ice spheres
		overall	longer	shorter	
0.005	44 ± 3	105 ± 11	135 ± 19	75 ± 8	50 ± 7
0.05	33 ± 2	91 ± 19	125 ± 25	53 ±8	55 ± 2
0.5	26 ± 2	48 ± 4	65 ± 6	31 ± 2	39 ± 4

247 **Table 1.** The average diameters (and their standard errors of the mean) of the ice crystals on the surface of the frozen samples
248 prepared from the 0.005 M, 0.05 M and 0.5 M CsCl solutions via the three freezing methods. The ice crystals in the seeded
249 samples had oblong shapes; therefore, the average sizes of the longer and shorter sides of the crystals were evaluated
250 separately. The number of crystals used for the analysis is presented in SI (Table S1).

251 In our experiments, the freezing of the seeded samples promoted the slowest freezing rates as
252 the ice crystals developed from a solution with a low degree of supercooling (the temperature of the
253 droplet was −2 °C) and the progress of the crystallization front could be observed with the naked eye.
254 This freezing technique produced the largest ice crystals. The freezing rates for the non-seeded
255 samples and ice spheres were much higher compared to those in the previous case, where
256 substantially smaller ice crystals had been produced. The ice crystals in the non-seeded samples and
257 in the ice spheres were about half the size of those in the seeded samples.
258 Our examination of the large crystals at low supercooling is parallel to the findings by Macklin and
259 Ryan, who investigated large crystal discs at low supercooling of pure water (Macklin and Ryan, 1966).
260 Their observation is explained by faster growth of the prismatic crystal plane in contrast to the basal
261 plane; thus, in the given case, the crystal grows preferentially in the direction perpendicular to its c-

262   axis. On the other hand, higher supercooling facilitates crystal growth also on the basal plane, resulting
263   in vigorous growth and complex shapes of the crystals. Such a condition then possibly leads to the
264   development of dendrites (Macklin and Ryan, 1966). The patterns in our micrographs illustrate this
265   claim suitably: low supercooling (Figure 2b) shows large disc-like crystals, whereas 16-degrees
266   Centigrade supercooling (Figure 21a) results in numerous small crystals. The fact that faster freezing
267   rates promote a high number of small ice crystals and slower ones form a few large ice crystals is well
268   recognized and efficiently utilized by productive freezing and lyophilization techniques (Kasper and
269   Friess, 2011;Jameel, 2010;Cao et al., 2003).

270   As mentioned above, the ice crystal size difference between the samples frozen under high and
271   low supercooling was expected. However, we were rather surprised that the ice crystals in the non-
272   seeded supercooled droplet were smaller than those in the ice spheres prepared by spraying a solution
273   into LN. Although LN boils at the very low temperature of −196 °C, its ability to cool the sample quickly
274   is reduced due to the inverse Leidenfrost effect (Adda-Bedia et al., 2016). Therefore, based on
275   analyzing the crystal sizes, we can infer that the spontaneous freezing of the non-seeded droplet
276   supercooled to about −16 °C occurred at the highest freezing rates experimentally attempted in this
277   study.

278   Another aspect affecting the crystal size consists in the concentration of the solutes. Generally,
279   the ice crystals were smaller when the solute concentration had increased. The observation is in
280   accordance with the conclusion proposed by multiple natural ice-core studies, namely, that high-
281   impurity ice exhibits, as a rule, smaller grains than low-impurity ice at the same depth (Eichler et al.,
282   2017). The explanation of this phenomenon may relate to the solution viscosity because ice crystal
283   growth depends on the diffusion of the water molecules to the crystal surface, and an increase in the
284   viscosity hinders the crystal growth (Braslavsky, 2015). The CsCl solution viscosity increases at
285   concentration values higher than approximately 2 mol kg^{-1} (Goldsack and Franchetto, 1977;Nakai et
286   al., 1995). The concentration in the veins of the freezing CsCl solution is expected to be within such a
287   range as the eutectic composition corresponds to about 7.7 mol kg^{-1} (Gao et al., 2017). A further factor
288   influencing the ice crystal sizes possibly relates to a decreased heat capacity of the solution due to the
289   presence of a solute (Bonner and Cerutti, 1976;Gao et al., 2017); thus, the solution may be cooled
290   more effectively and the ice may propagate at a quicker pace, leading to smaller ice crystals. Changes
291   in the above-described aspects could also cause altered microscopic convection patterns within the
292   sample being frozen; these were previously shown to play a major role in the freezing of macroscopic
293   quantities of sea water (Wettlaufer et al., 1997).

294

295   3.3 Brine on the surface of the frozen samples

296   **3.3.1 Effects of the salt concentration.** Typically, the brine on the surface of the frozen samples
297   increased in amount with rising concentration of the salt. Such behavior is not surprising as the
298   maximum concentration of a salt in the brine and the proportion of the brine to the ice at each
299   temperature are given by the liquidus curve in the phase diagram; the amount of the liquid brine
300   increases with the salt concentration and temperature.

301   The grain boundary grooves became substantially thicker when the concentration had increased.
302   The average widths of the brine-filled grain boundary grooves related to the concentration are given
303   in Table 2. The measurements are displayed in S17. The average groove widths for the 0.005 M samples
304   might be overestimated as many grooves were so thin that they were almost invisible or their widths
305   approached the image resolution (approx. 0.5 μm). The grain boundary grooves could not be
306   determined for the non-seeded sample with the CsCl concentration of 0.5 M, as the ice crystals were
307   barely visible below the brine layer; the layer covered nearly the whole surface of the sample.

308

Concentration of CsCl / M	Average width of the grain boundary grooves / µm		
	Non-seeded samples	Seeded samples	Ice spheres
0.005	1.34 ± 0.49	1.09 ± 0.33	1.16 ± 0.34
0.05	2.06 ± 0.87	1.12 ± 0.29	1.88 ± 0.53
0.5	ND	5.7 ± 2.0	3.3 ± 1.1

309 **Table 2:** The average widths of the CsCl brine-filled grain boundary grooves for the frozen samples prepared from the 0.005 M,
310 0.05 M, and 0.5 M CsCl solutions via the three freezing methods. The uncertainties represent the pooled standard deviations.
311 The numbers of independent samples used for the calculation are listed in SI (Table S2). The average width of the grain
312 boundary grooves for the 0.5 M non-seeded sample was not determined, as the brine layer had covered almost the whole
313 surface of this sample.

315 **3.3.2 Impact of the freezing method on the surface coverage.** The brine surface coverage in relation
316 to the freezing method was estimated for the frozen 0.05 M solutions. While the brine covered (18.2
317 ± 4.0) % and (9.0 ± 2.8) % of the surface in the non-seeded and the seeded samples, respectively, it
318 occupied only (4.1 ± 1.5) % in the ice spheres (Table S3). These estimates are based on the detected
319 relative brine surface coverage in 5 independent samples for each freezing method. However, the
320 estimated surface coverage might be strongly dependent on the intensity of the detected signal, as
321 discussed in the Methods section. Therefore, the only item of information we can extract is the
322 normalized brine surface coverage. Regrettably, neither the thickness of the brine layer nor the
323 absolute amount of the salt on the surface can be evaluated using the ESEM.

324　　The location of the CsCl brine within the sample and the related surface coverage were
325 presumably dependent on the freezing rate and its directionality. In the globally supercooled non-
326 seeded sample (cooled with a Peltier stage from the bottom), we suppose the crystallization was
327 directed from the bottom upwards, as shown previously by Suzuki et al. (2007) for a supercooled water
328 droplet on a silicon surface; thus, the salt was prevalently expelled from the bulk to the surface of the
329 sample as the abrupt crystallization proceeded. Conversely, the seeded sample probably started to
330 crystallize from the surface, close to the edge of the sample as the first place in touch with the seeding
331 crystals. Because the given freezing method promoted the slowest freezing rates, we assume that most
332 of the salt was expelled from the growing ice towards the bottom of the frozen sample. Thus, only a
333 small portion of the salt could be seen on the surface. The lowest brine surface coverage was detected
334 in the ice spheres created by the freezing of micrometric droplets from the surface inwards;
335 apparently, the CsCl solution was expelled by the growing ice from the surface of the sphere towards
336 the centre and the CsCl brine inclusions were trapped below the surface. Other arguments supporting
337 this assumption are presented in the chapter discussing the interior of the frozen samples.

339 **3.3.3 Effects of the temperature.** As regards the seeded droplet of the 0.005 M CsCl solution, the brine
340 surface coverage was studied as a function of temperature (Figures 3, 4, Movie S1). For this sample,
341 about 20% of the surface was covered with the CsCl brine, initially at −23.4 °C. Note that such surface
342 coverage is, unexpectedly, larger than that found on average in the more concentrated seeded sample
343 (c = 0.05 M) within the previous section. The explanation may lie in the stochastic behavior of the
344 freezing process; however, we identify the most important factor in the difference of the instrumental
345 settings, which, for reasons already outlined above, does not allow quantitative comparison of the
346 micrographs. The brine was located mainly on the ice surface humps (Figure 3).

347　　When the temperature was gradually increased, the area of the brine-covered surface grew larger
348 (Figure 4). Such behavior was expected as the liquid fraction in the partially frozen sample increases
349 with the temperature in the region between the T_{eu} and the melting point. At the highest temperature
350 examined, −12 °C, about 80% of the surface was covered with the brine. Subsequently, the

9

351 temperature was abruptly lowered from −12 °C to −23.3 °C, and the brine surface coverage fraction
352 decreased from about 80 % to approximately 40 %.
353 According to the CsCl-water phase diagram (Figure 1), the equilibrium concentration of the CsCl
354 brine equals 7.7 mol kg^{-1} at −23 °C and 3.9 mol kg^{-1} at −12 °C (Gao et al., 2017), meaning that if a
355 constant amount of the CsCl salt on the surface is assumed, the brine volume on the frozen surface
356 should approximately double after the temperature had increased from −23 to −12 °C. Even though it
357 is not possible to evaluate the volume from the microscopic images, we documented well that the
358 brine surface coverage had risen four times during the warming, becoming much larger than the
359 coverage implied by the phase diagram.
360
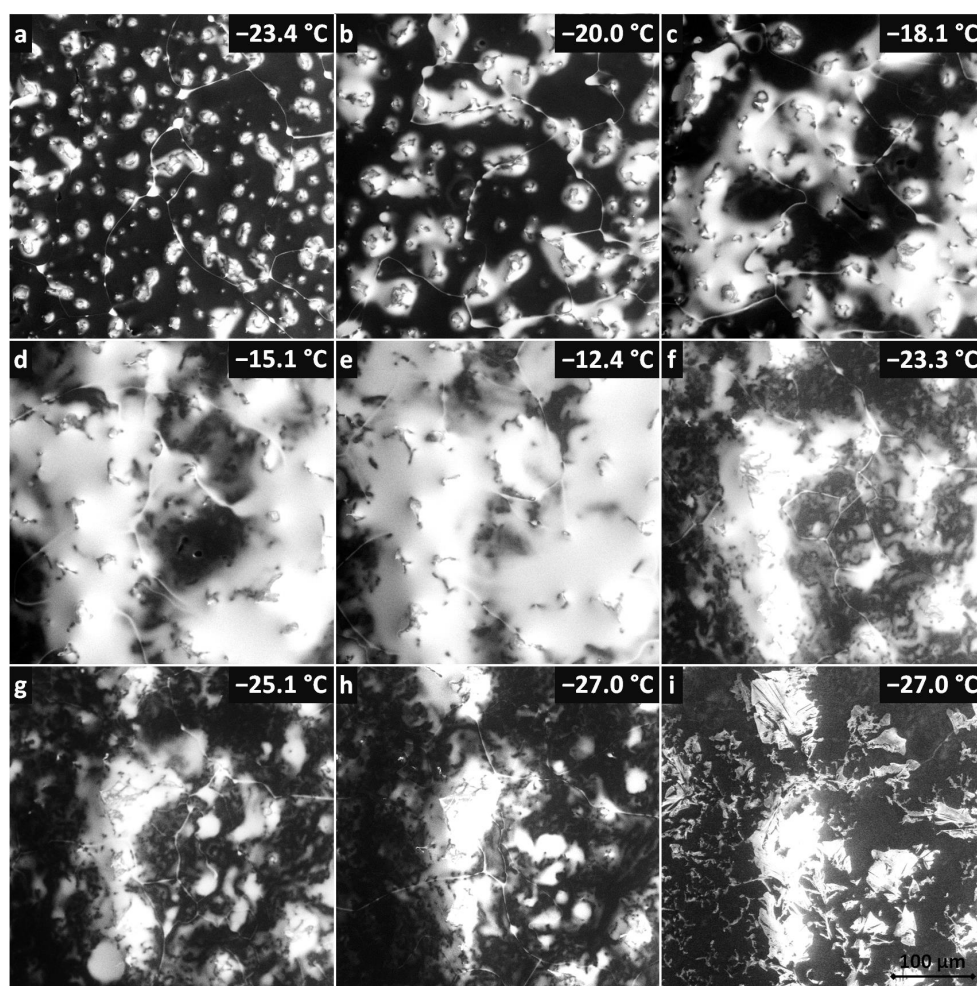
361
362 **Figure 3.** The brine surface coverage as a function of temperature for the seeded 0.005 M sample. The temperature was first
363 increased stepwise from −23.4 °C to −12.4 °C and then decreased to −27 °C. The procedure took 30 minutes (Figure 4). A
364 movie from this experiment is included in the Supplementary material section (Movie S1). The panels h and i display the salt
365 crystals forming from the brine. The crystals formed along the grain boundaries and on the humps where the brine had
366 accumulated previously. The crystallization started a minute after the sample holder temperature had been set to −27 °C.
367 The air pressure in the microscope chamber was 500 Pa during the sequence. The scale in panel i is valid for all the images.

368
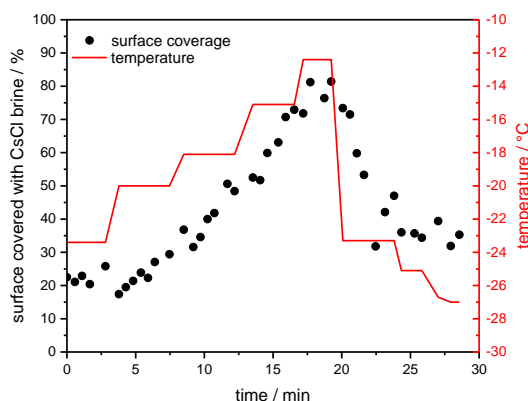
10

Figure 4. The brine surface coverage in the frozen seeded droplet (c(CsCl) = 0.005 M) at varying temperatures. The representative images used for the calculation are displayed in Figure 3.

During the cooling phase, the decrease of the brine by half was expectable, considering the phase diagram; however, the surface coverage at the end of the experiment was significantly larger compared to the initial stage, despite the essentially equal temperatures (−23.4 °C vs. −23.3 °C). Moreover, the temperature decrease down to −27 °C at the end of the experiment led to a surface coverage of about 30%, which, despite the temperature being 3.6 °C lower, exceeded the amount of coverage found at the initial stage by 10 %.

The results of this temperature cycling experiment indicate that, as the ice from the surface was required to melt during the heating in order to double the volume of the brine, a formerly inaccessible portion of the brine (restrained due to being trapped below the surface layer of the ice) surfaced. This increased the amount of the CsCl salt on the surface, and the brine volume rose dramatically above the expectations stemming from the phase diagram. The subsequent cooling of the sample lowered the volume by half, as expected; thus, the overall amount of the CsCl salt on the surface did not change at the cooling stage. This observation implies that the temperature cycling may result in enhanced accumulation of the brine on the frozen surface during the heating phase.

In the experiment, the CsCl started to crystallize from the brine at −27 °C only after a time delay (Figure 3i). The salt crystallization front propagated along the brine-filled grain boundaries and puddles (Figures 3, S3, Movie S1). The salt crystals exhibited a fine dendritic structure. We are currently investigating the details of salt crystallization and ice sublimation in salt-containing samples under various conditions.

Having set the cooling stage to −25 °C, we observed the brine to supercool at first, with the crystallization occurring only after a prolonged period. The hitherto published T_{eu} values of the CsCl-H_2O mixture range from −24.83 to −22.3 °C (Cohen-Adad, 1991;Dubois et al., 1993;Fujiwara and Nishimoto, 1998;Monnin and Dubois, 1999;Chen et al., 2005;Gao et al., 2017). It cannot be excluded that the sample surface was several degrees warmer than the holder due to the effects of the electron beam; purging relatively warm gas through the specimen chamber; and limited thermal conductivity of the sample. During the experiment, the sample surface was cooled by the ice sublimation and water evaporation from the brine. These factors could contribute to the salt crystallization on the sample surface, even when the temperature of the holder does not change; still, the surface of the frozen samples might be about 2 °C warmer than the holder, as already discussed in the experimental part.

11

402   The observed ice surface coverage changes have consequences for the interaction with radiation
403   under natural conditions: the higher the brine volume on the ice surface, the more absorbing the
404   surface compared to the condition of dry ice surface, which is highly scattering (Light et al., 2009).
405   Thus, the temperature increase with the subsequent spread of the brine on the surface may lead to
406   the surface darkening, resulting in higher solar radiation absorption and further increase of the
407   temperature. Conversely, the brine crystallizing on the ice surface would result in larger reflection of
408   the radiation as the crystals would scatter the light substantially more effectively compared to the
409   liquid brine.

410

411 ### 3.4 Formation of the humps
412   The surface humps were observed in the numerous non-seeded and seeded samples, often in co-
413   location with the brine puddles. The time-lapse images revealed the humps forming at places where
414   the puddles had been located previously (Figure 5). The humps usually exhibited broader bases and
415   thin tips; the brine was located mainly at the bases, not on the tips (Figures S4, S5). As the sublimation
416   continued, the tips became even thinner. In some cases, the thin tip separated from the body of a
417   hump and fell off (Figure S4). From these observations we infer that the humps are predominantly
418   formed during microscopic examinations due to ice sublimating from the frozen samples; we do not
419   expect the humps to be originally present on the surface of the samples. The formation of the humps
420   appears to be facilitated by the brine puddles on the ice surface: when the surface is covered with the
421   brine, the sublimation from the given spot is retarded, and a hump is formed. Such formation might
422   be an artefact caused by experimentation in a low-pressure environment. Previously, similar
423   observation had been explained in terms of charged peaks formed by etching in the SEM (Barnes et
424   al., 2002).
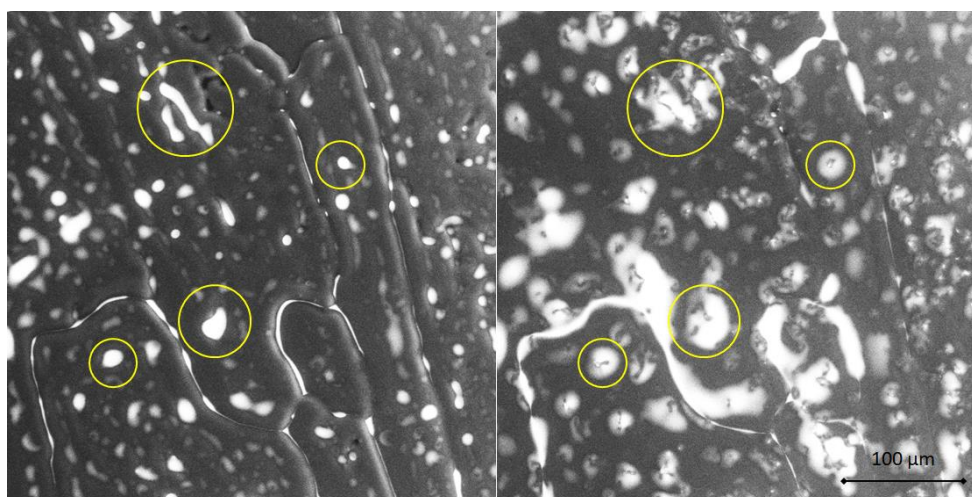
425
426 **Figure 5.** The ESEM images of the seeded sample prepared from the 0.05 M CsCl solution at the very beginning of the
427 observation (left panel) and after 90 s (right panel). The images were recorded at the temperature of −25 °C. As conditions
428 below the sublimation curve had been set inside the specimen chamber, sublimation of the top layer of the ice was presumed
429 during the time interval between two images. It is clearly visible that the humps formed at spots previously covered with the
430 brine; four examples of such spots are encircled.

431 ### 3.5 Dynamics of the ice surface
432   The dynamics of the frozen samples' surfaces could be observed even at −23 °C. The CsCl brine-filled
433   grain boundaries were not static: their positions changed swiftly in time. Interestingly, the positions of

434   the humps on the ice surface did not change accordingly. A representative example is shown in Figure
435   6 and Movie S1. The surface of the seeded droplet from the 0.005 M CsCl solution was observed at
436   −23.4 °C. As is demonstrated by the yellow arrow, whose position remains constant in all the panels in
437   Figure 6, the indicated hump was originally encircled by brine-filled channels (panel a). We suppose
438   the channels denote the ice grain boundary positions. With the time progressing, the grain boundary
439   on the right-hand side gradually moved through the hump, while the appearance of the hump did not
440   change. It was also observed that the humps caused the directional propagation of the ice boundaries
441   to decelerate; several such examples are presented in Movie S1. A larger brine volume is noticeable at
442   the triple junctions of the ice grains. The dynamics of the process together with the sampling relatively
443   slow compared to the ice boundary movement lend the brine reservoirs the appearance of
444   propagating comet-like objects; this effect is demonstrated via the related encircled points in Movie
445   S1. These brine pools occasionally appear at the locations of caverns formed by bubbles, thus
446   delineating the grain boundary, which would otherwise be difficult to observe.
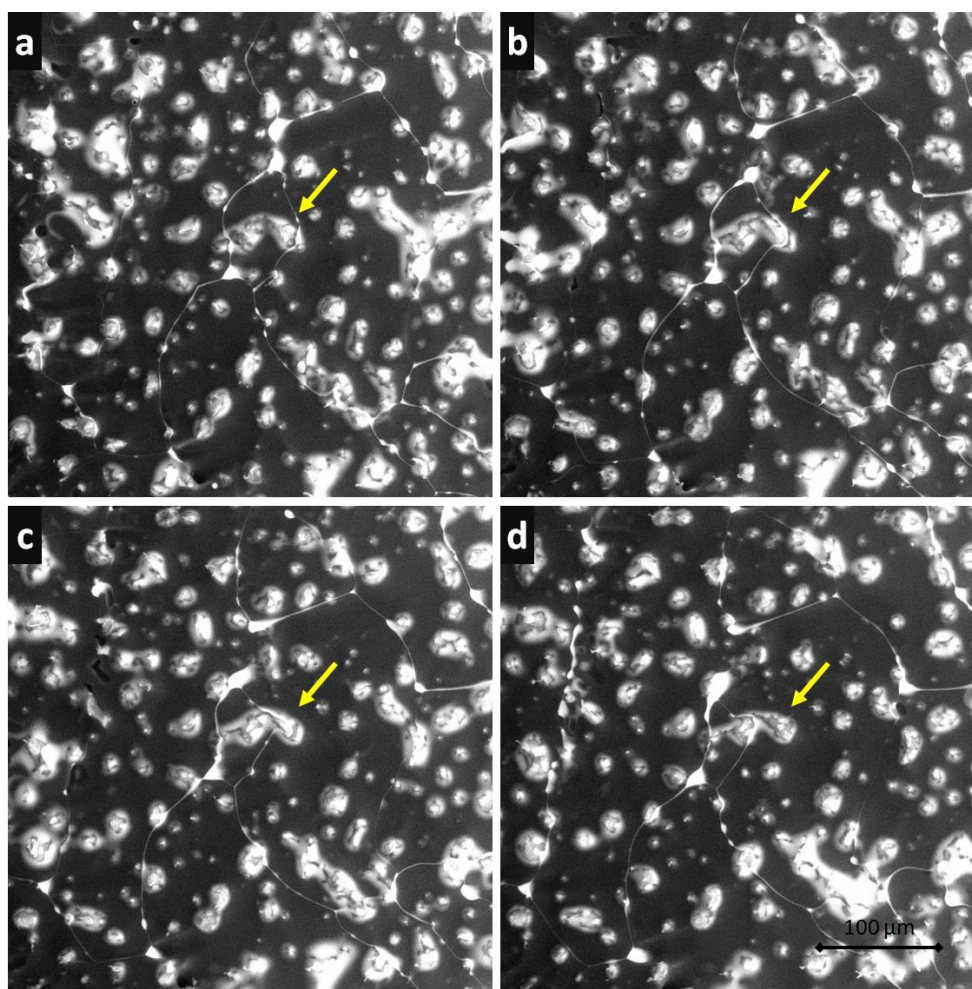
447
448 **Figure 6.** The ice surface dynamics observed at −23.5 °C and 500 Pa. The brine-filled grain boundaries (white channels) shifted
449 their positions in time, while the positions of the humps did not change. An example is indicated by the yellow arrow pointing
450 to a CsCl-filled channel moving through a hump. The arrow indicates the initial position of the brine channel in all of the

13

451 figures. The sample was prepared from the 0.005 M CsCl solution by freezing a droplet seeded with ice at −2 °C. The time
452 interval between the images is approximately 30 s. The scale in panel d is valid for all of the images.

453

454 The fact that ice is a very dynamic medium allowing reconstitution at sub-zero temperatures was
455 previously evidenced using, for example, time-lapse X-ray tomography; up to 60 % of the total ice mass
456 recrystallized during 12 hours at − 15 °C (Pinzer and Schneebeli, 2009;Hullar and Anastasio, 2016). Our
457 research team is not the first one to have observed disjoint behavior of the ice surface in relation to
458 the underlying ice crystals; fresh ice growing in steps of 100 − 4,000 nm to traverse the ice grains
459 regardless of the boundaries was already noticed for planar ice growth (Ketcham and Hobbs, 1968).
460 Moreover, the observed mutual interactions between the surface humps and the ice grain boundaries
461 causing temporal retardation of the boundaries and partial draft of the hump (in the direction of the
462 boundary motion) can be classified as Zener slow-mode pinning (Eichler et al., 2017). New ice grain
463 formation (probably ascribable to the grain-boundary bulges mechanism) and the subsequent ice
464 crystal growth are visualized in Figure 7 (Steinbach et al., 2017). In this context, however, another
465 explanation is also acceptable, as discussed below.
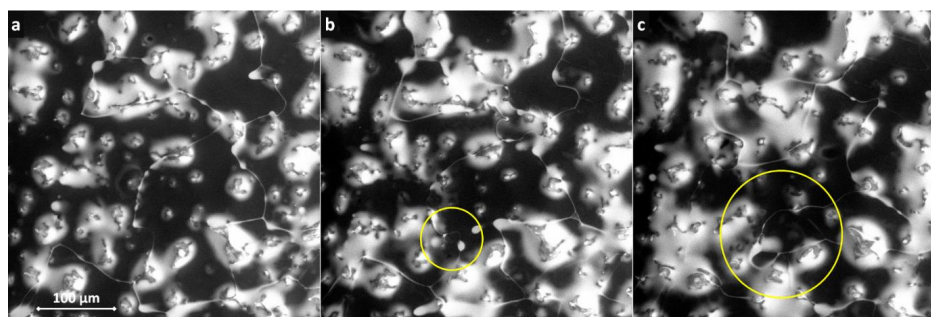
466
467 **Figure 7.** The ice surface dynamics observed at −23.5 °C and 500 Pa; newly formed ice grains are encircled.
468
469 The actual reason why the brine channels were dynamic while the humps remained static is not
470 entirely clear to us. The causes of the recrystallization process are nevertheless appropriately
471 summarized by Steinbach; the relevant factors include the thermal gradients and strains in the samples
472 (Steinbach et al., 2017). Two possibilities are considered in this respect:
473 Firstly, the movement of the brine channels could be induced by a temperature gradient across
474 the surface of the frozen ice. The sample was prepared from a hemispherical droplet by cooling from
475 the bottom. Thus, the height was most likely not constant across the sample and would be the most
476 prominent in the center, allowing the temperature gradient to rise across the surface. The surface in
477 the middle portion of the sample was supposed to be warmer compared to the peripheral sections as
478 the gas flow entering the ESEM chamber was relatively warm. Under a temperature gradient, the
479 solute would exhibit higher concentration at the colder end of the brine inclusion and lower
480 concentration at the warmer end, resulting in migration of the brine inclusions toward the warmer
481 region of the ice (Light et al., 2009). The behavior observed in the present study indicates that the
482 water molecules at the brine-filled grain boundaries are redistributed much faster than those on the
483 ice surface. The dissolved salt may diffuse through the veins to increase the salt concentration on one
484 side and decrease it on the other. Where the concentration increases, the ice grain boundaries will
485 melt, and where it decreases, the ice will grow to maintain equilibrium conditions.
486 A second hypothesis to explain the apparent movement of the brine channels focuses on the ice
487 sublimation from the sample surface. The brine channels were not necessarily perpendicular to the
488 surface; the angle between the surface and the channels was low, and therefore the sublimation of a

14

489 thin layer of ice from the surface could theoretically result in apparent movement of the brine channels
490 while the appearance of the humps would not change markedly. Similar reasoning had been employed
491 for the sublimation of not perpendicularly oriented ice crystals to explain the observed excessive width
492 of the ice-grain grooves (Cullen and Baker, 2001). We are, however, uncertain if the reason for these
493 unusual dynamics of the frozen surface consists in one of the previously described conditions, both of
494 them, or a completely different process.
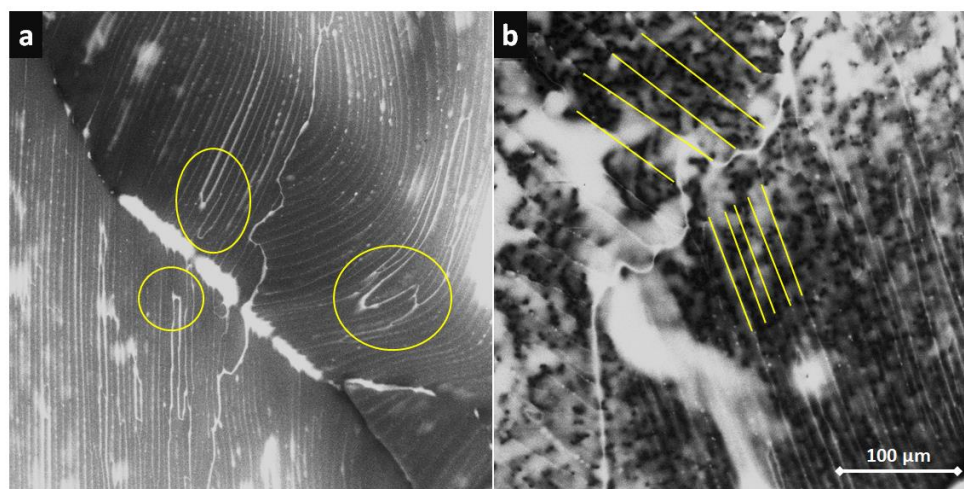
3.6 Interior of the frozen samples

496 **3.6.1 Sublimation.** The subsurface structure of the samples was revealed after partial sublimation of
497 the ice from the surface made from the 0.005 M CsCl solution (Figure 8). Subsurface hollows were
498 observed in all types of samples, namely, the non-seeded and seeded ones as well as the ice spheres.
499 The numbers and sizes of the hollows nevertheless differed: the hollows in the non-seeded samples
500 were small (units of micrometers) but numerous; those in the seeded samples were scarce; and those
501 in the LN-prepared ice spheres were numerous, with the size varying from units to one hundred
502 micrometres. The formation of these hollows is presumably associated with air bubbles trapped below
503 the ice surface. For all the freezing methods, opening the hollows by further sublimation often revealed
504 them to be partially filled with the brine (Figure 8); the co-location of the brine with gases suggests
505 that the brine in the veins is air-saturated. The presence of gases in the brine had been shown
506 previously to ease the crystal recrystallization and ice boundary migration (Harrison, 1965). Recently,
507 brine inclusions trapped below the ice surface co-located with air bubbles were found (Hullar and
508 Anastasio, 2016). The co-location of the brine and the bubbles was most pronounced for the ice
509 spheres, formed by freezing microdroplets of the solution by LN at temperatures close to 77 K. The ice
510 spheres were most likely frozen from the surface inwards; therefore, the entrapment of the brine and
511 air inside the structure was anticipated as was also observed prepared fractured samples in similar
512 manner (McCarthy et al., 2013). Conversely, the method of seeding allows the expulsion of most of
513 the impurities (air, brine) out towards the surface.

Method of freezing

| No seeding | Seeding | Ice spheres |
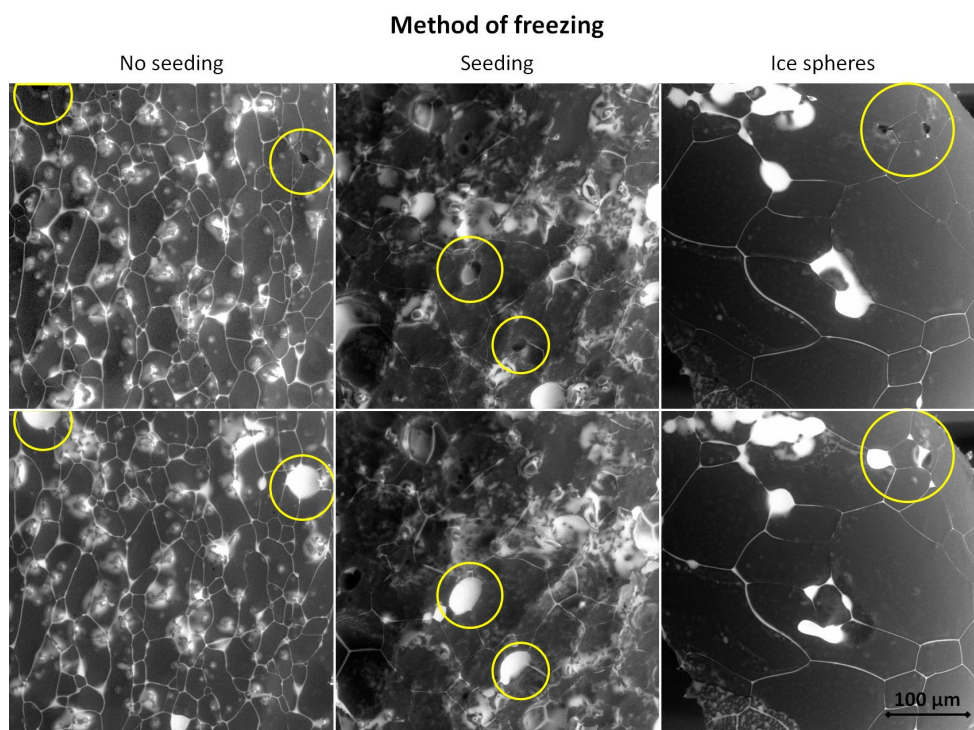
Figure 8. The ESEM images of the partially sublimed frozen samples prepared from the 0.005 M CsCl solution: the non-seeded droplet (left, −25 °C); the seeded droplet (middle, −25 °C); and the ice sphere (right, −23 °C). The hollows in the internal structure were revealed after the initial sublimation of the ice from the surface (upper panels). Further sublimation showed the hollows filled with the brine (lower panels); the time interval between the upper and the lower images was about one minute. The grey areas represent the ice, while the white regions indicate the CsCl brine.

3.6.2 Fragmentation. An additional method to observe the interior of a frozen sample consisted in fragmenting the LN-frozen macroscopic ice samples and inspecting the pieces originated from the given interior in the ESEM. Representative images of the fragments are displayed in Figure 9; it is clearly visible that the ice and the brine are arranged in parallel lamellae in the original interior of the fragmentized sample. The brine lamellae appear as lines on the micrograms. These lamellae were approximately equidistant within one facet of the fragment; however, when various facets are compared within one sample, the distances between the lamellae might differ significantly. The closer brine lamellae spacing for the lower-right facet in Figure 9b was approximately 10 μm; the wide-spaced arrangement (at 40 μm) is displayed on the upper-left facet. The lamellae were long and narrow. Sparsely, the parallel structure of the lamellae was interrupted by the bridge connecting two adjacent brine layers across the ice plate; several examples of these are encircled in Figure 9a. Only few bridges were typically recognized on the individual facets. We cannot determine if these features were present in the samples naturally or through the sample fragmentation (Maeda et al., 2003).

Figure 9. The interior of the fragmentized LN-frozen sample of 0.05 M CsCl imaged with the ESEM at −25 °C. The grey areas represent the ice, and the white regions indicate the CsCl brine. The brine was arranged in densely spaced parallel lamellae. Bridging of the ice was rare within a facet; examples of the effect are highlighted in panel a. The brine lamellae were equidistantly spaced within a facet. However, the distances between the lamellae might differ significantly among the facets (b). Images of two additional samples for this freezing method are provided in SI (Figure S16).

The structures observed in the interior of the LN-frozen samples resembled the lamellar eutectic structure of alloys (Losert et al., 1998;Yan et al., 2017) or the pattern often recognized when sea ice is formed (Anderson and Weeks, 1958;Petrenko and Whitworth, 1999;Weeks, 2010;Thomas, 2017;Nagashima and Furukawa, 1997). This pattern is generated due to the constitutional supercooling of the liquid ahead of the freezing interface. It has long been known that the fastest freezing produces dendritic structures, whereas gradual slow freezing is characterized by cellular and planar structures, respectively (Rohatgi and Adams, 1967;Trivedi and Kurz, 1994). As a matter of fact, the microscopic structure of ice and brine is a complicated function of the thermal gradient and rate of freezing (Losert et al., 1998;Yan et al., 2017;Maus, 2007). The spacing of the parallel lamellae of pure ice separated by brine layers, created in a direction perpendicular to that of freezing, is characteristic of particular freezing rates and salt identities and concentrations. In terms of freezing salts solutions (NaCl, KCl and LiCl), the spacing between the perpendicular lamellae was experimentally found to be proportional to the inverse square root of the freezing rate (Rohatgi and Adams, 1967). The same paper reported that the maximum freezing rate, as well as its average, was inversely proportional to the square of the distance from the chill. At the same time, an increase of the solute concentration is responsible for the larger spacing between the lamellae. It is therefore conceivable that the uneven spacing observed in Figure 9b is due to unequal temperatures and/or concentrations for the growth of the individual ice facets. Another contributing factor could be the altered relative angle of the facets towards the detector, which would result in biased observed spacing.

It is interesting to note that lamellar brine arrangement was not observed in any other sample, namely, neither on the surface of the LN-frozen macroscopic sample (Figure S6) nor on or below the surface of the ice spheres (Figures 2 and 8, right-hand columns). Instead, structures more resembling cellular arrangement rather than lamellar interface is formed for the small samples (Weeks, 2010;Losert et al., 1998). We can only speculate if the absence of lamellar growth in the micrometric ice spheres is due to the higher freezing rate or exposure to a lower temperature gradient compared to the macroscopic sample with the diameter of 8 mm immersed in LN. Two significantly different ice sample structures were observed, even though LN was used as the coolant in both cases. A recent study of the inverse Leidenfrost effect of levitating drops on the surface of LN revealed strong

17

567 dependence of the freezing time on the size of the droplet (Adda-Bedia et al., 2016); therefore, the
568 size and surface properties of micrometric ice spheres in contrast to those of gelatine capsules can be
569 among important contributing factors as regards the described difference.

570

4 Relevance to previous observations

572 The ESEM observation presented herein employed a proprietarily developed detection system
573 allowing the use of very low currents (40 pA) and short dwell times (14 µs) to minimize the samples'
574 degradation during the imaging (Nedela et al., 2018). The electric field was not found to influence the
575 ice growth (Rohatgi et al., 1974). There was a subtle magnetic field present in our microscopic
576 chamber. Thus, our observations differed from the natural conditions mostly due to the low pressure
577 of 500 Pa inside the chamber.

578   In the experiments, CsCl was used as the solute thanks to its high contrast between the caesium
579 atom and the oxygen and hydrogen of ice when BSEs are detected. It served as the model compound
580 for monovalent chlorides, abundantly present in the environment. CsCl solutions exhibit properties
581 relatively similar to those of NaCl ones; in particular, the eutectic temperatures important for this study
582 are very close to each other (T_{eu} (CsCl) = -23 °C, T_{eu} (NaCl) = -21.21 °C) (Brady, 2009). The tested
583 concentrations ranged over two orders of magnitude. The value of 500 mM approaches the
584 concentration of NaCl in seawater, and therefore it also corresponds to that of fresh sea ice (Massom
585 et al., 2001;Thomas, 2017). NaCl concentrations reaching up to 160 mM were detected immediately
586 next to a highway treated against road icing; 50 mM of a salt solution can thus be considered a
587 concentration potentially found farther from roads or also in their close vicinity when the salt was
588 already partly flushed away (Notz and Worster, 2009;Labadia and Buttle, 1996). The 5 mM value
589 corresponds to that discovered in surface snows in arctic coastal regions or on the surface of frost
590 flowers (Beine et al., 2012;Douglas et al., 2012). A similar concentration had been used in the report
591 on solute locations in ice by Hullar and Anastasio (2016).

592   The principal finding presented within our study is embodied in the very strong sensitivity of the
593 ice-brine morphology and brine distribution to the freezing method (Figure 2, 3). Even for identical
594 solution concentrations, the method and direction of freezing strongly modify the appearance of the
595 ice surface morphology. In all of the experiments, we observed a clear difference between the
596 interconnected system of the brine in the grain boundary grooves and the predominantly separated
597 brine puddles. At the lowest salt concentrations, free ice surfaces dominated. As the concentration
598 rose, the grain boundary grooves broadened, and both the amount and the size of the brine puddles
599 increased; however, some parts of the surface would remain bare even at the highest concentrations.
600 Partial surface wetting had been invoked previously (Domine et al., 2013).

601   The directionality of freezing influences to a large extent the amount of brine exposed on the
602 surface. Freezing from the outside inwards segregates the brine inside the ice matrix, whereas the
603 same process starting from the bottom expels the brine to the ice surface. The directionality of freezing
604 was previously shown to play a key role in determining the final distribution of impurities at the
605 macroscopic scale for the formation of ice on seawater (Wettlaufer et al., 1997). With the samples
606 cooled from the top by air at -20°C, it was observed that the salt is retained in the mushy layer of ice
607 until it reaches a critical height. After this stage, plumes (capsules) of a saturated salt solution (having
608 a higher density and low temperature) migrate downwards, leaving space for a less concentrated
609 solution and thus faster growth of the ice. The role of material convection in relation to the drop size
610 may thus have to be considered for the modeling of the freezing process.

611   The distinct ice grain sizes and textures shown for the various freezing methods (Figures 2, 8, 9,
612   and Table 1) indicate possible differences in the mechanical, thermal, and optical properties of the ice,
613   influencing, for example, the samples' permeability for percolating solutions or their optical properties.
614   Related changes could affect numerous properties of ices, having geological consequences such as the
615   impact on sea ice desalination and melting; further, the variations might influence also the energy
616   balance of ices and aerosols and rates of the (photo)chemical reaction (Thomas, 2017). In our
617   experiments, the samples were invariably placed on the silicon pad in the microscope. This procedure
618   renders the observation different from that of natural sea ice, where the brine from the ice may leak
619   into the seawater (Notz and Worster, 2009). Nevertheless, our observations can be considered a good
620   model for salty ices on solid grounds.

621   The ice sublimation effects displayed in Figure 8 suggest the character of the behavior of salty ice
622   samples exposed to dry winds in the nature. Gradual brine accumulation is expected.

4.1 Connection to previous microscopic observations

624   In previous studies of frozen aqueous solutions, two regions were described: one of the
625   uncontaminated, pure ice matrix, and the other with impurities concentrated in liquid-like
626   compartments above their eutectic temperatures (Krausko et al., 2014;Thomas, 2017;Lake and Lewis,
627   1970;Rohatgi and Adams, 1967). The impurities' inclusion was observed via several microscopic
628   methods for both laboratory-prepared samples and natural ice and snow. However, the imaging
629   methods reaching -20°C or more did not have a resolution large enough to visualize the impurities in
630   the grain boundary grooves and were blind to the ice topography. For this reason, the impurities in
631   the grain boundary grooves of polycrystalline ices had been previously observed in high vacuum by
632   low temperature (< -80 °C) SEM (Barnes et al., 2003;Cullen and Baker, 2001;Blackford et al.,
633   2007;Rosenthal et al., 2007). Our technique facilitates the observation of all the aspects: the liquid
634   brine puddles, brine in the grain boundary grooves, and, to some extent, ice topology. The aim in this
635   context is to summarize the previous observations, with a focus on the dimensions of the observed
636   impurities' elements; first, attention is paid to the veins of subtle impurities and grain boundary
637   grooves and, second, the larger puddles are discussed.

4.1.1 Observing the grain boundary grooves and veins

639   Typically, in the procedures adopted to observe the impurities, the ice samples were repeatedly
640   exposed to "etching ", e.g., ice sublimation at a higher temperature (-20 °C)(Rosenthal et al.,
641   2007;Cullen and Baker, 2001). The analysis allowed examination of pure ice crystals surrounded by
642   veins containing the impurities. Using the energy dispersive X-ray technique, the veins were found to
643   contain elements (e.g., Cl, S, Na, Mg) corresponding to the common minerals (NaCl, sulfates) for
644   natural glacier samples (Cullen and Baker, 2001). At certain instances, the grain boundary impurities
645   would coagulate to form filaments that can eventually peel off the ice due to differing thermal
646   expansion coefficients. The diameters of the filaments varied between 0.2 and 2.5 μm, and the
647   dimension of the nodes (the meeting points of four grains) was approximately 5 μm (Blackford et al.,
648   2007;Rosenthal et al., 2007). However, the diameter of the groove formed by the sample sublimation
649   at 253 K for 8 weeks reached as high as 250 μm. The apparent size of the sublimation groove can be
650   biased by the fact that the ice crystals do not need to be oriented perpendicularly to the plane of
651   observation. The observation most relevant to the ice spheres presented herein is that of the NaCl
652   solution (0.043 M) nebulized into LN and observed at -120 °C (Blackford et al., 2007). The newly
653   prepared ice spheres exhibited sub-micrometer fine filaments of salt on the surface, whereas sintering
654   at -25 °C allowed separated patches (up to 100 μm in diameter) and filaments threading the ice crystals
655   due to metamorphism (Blackford, 2007;Domine et al., 2013). Further sublimation of the ice striped the

19

656 filaments and showed that they form 3D interconnected structures, indicating also that each filament
657 has a star-like geometry, which is appropriately explained via considering the surface energies of the
658 ice and the brine.

659   All the dimensions of the veins observed previously correspond very well to those of the grain
660 boundary grooves reported in the present paper (Table 2). The grain boundary grooves are formed at
661 positions where two neighboring ice grains meet on the ice surface; thus, they thread each individual
662 ice grain. Apparently, the amount of the brine on the ice surface was not sufficient to fill the groove
663 around all the ice grains due to low brine concentration and/or the freezing method concentrating the
664 brine towards the interior of the ice matrix (Figure 2c, e, f). Even for the most concentrated samples,
665 the grain boundary grooves were found to range below 6 μm on average. The ice grain boundary
666 grooves were predicted to increase their width with rising temperature and upon aging; (Nye, 1991)
667 for example, under certain conditions, the values of 0.3 mm and 0.7 mm are assumed after 10 and 100
668 days, respectively, at 0 °C.

4.1.2 Observation of the brine puddles

670 The advantage of optical microscopic methods and X-ray tomography consists in the possibility of
671 working at atmospheric pressure and an arbitrary temperature; the central drawback of these
672 approaches rests in the compromised special resolution (Blackford, 2007). Importantly, optical
673 microscopy maintains the transparency of ice to visible light, causing the image to include the
674 subsurface information (Eichler et al., 2017); this aspect can be considered a benefit or a drawback,
675 depending on the situation. Thus, the applied method relied on imaging the larger brine patches, but
676 the brine in the subtle ice boundary grooves could not be represented.

677   The fluorescence microscopy technique exploiting a pH indicator showed a major difference
678 between a frozen aqueous solution (without added salt) and a 0.1 mM solution of NaCl at -7 °C (Cheng
679 et al., 2010): the former left pools of the solution around the ice crystals (approx. 12 μm wide), whereas
680 the latter was specific in that the solute was mostly rejected towards the edge of the microscopic field
681 of view, leaving only a few thin brine channels in the bulk of the ice. Another study based on
682 fluorescence microscopy was intended to assess the amount of aggregation of bovine serum albumin
683 labelled by a fluorescence probe (Roessl et al., 2015). Fast freezing rates produced more puddles of
684 proteins, while slow ones led to fewer larger patches (millimeter sized), with the protein contained in
685 a more concentrated solution. Such results agree with those assessing the extent of aggregation via
686 the spectroscopy of methylene blue (Heger et al., 2005). The patches containing various salts were
687 shown, via X-ray fluorescence imaging, to increase their surface concentrations with decreasing
688 temperatures (Tokumasu et al., 2016). In the referenced study by Tokumasu et al., the patches were
689 determined to be about 30 μm wide at temperatures from -5 to -15 °C. The optical microscopy and
690 Raman spectroscopy of ice core samples detected microscopic impurities assigned to salt crystals and
691 dust scattered through the ice matrix (Eichler et al., 2017). Eichler et al's report did not find any signal
692 for liquid inclusions in the form of pools or veins around the ice grains at -15 °C. The resolution of the
693 microscopy corresponded to 3 μm/pixel, a value higher than the dimension of most of the grain
694 boundary grooves measured in our experiments. Therefore, it appears probable that the method did
695 not facilitate discerning the sub-surface ice grain boundaries (Eichler et al., 2017). Recently, the Raman
696 microscopy of ice revealed the dependence of the brine puddles' width on the temperature; the width
697 increased from 10 μm at -20 °C to 20 μm at -10 °C for 0.6 M NaCl solutions (Malley et al., 2018). Interior
698 images of laboratory frozen CsCl aqueous solutions (1 mM) were acquired with X-ray microtomography
699 (Hullar and Anastasio, 2016). Slow freezing in a refrigerator led to the formation of large pools of
700 impurities (tens to hundreds of micrometers), whereas dumping the sample into liquid nitrogen

20

701 produced small segregations, namely, ones sized below the voxel size of 16 μm. The impurities were
702 often associated with the air bubbles. The ice grain boundaries were not visualized as their dimensions
703 are below the resolution of the applied method. Quantification of the overall amount of the CsCl
704 present in the samples reveals that a substantial part of the CsCl is not detected in the analysis; thus,
705 it must be present in the sub-detection compartments in the bulk of the ice matrix. Based on the
706 current study, we suggest that the amount of missing brine can be located in the veins. A similar
707 conclusion was drawn in one of the first attempts to quantify the amount of air in ice, with the success
708 not exceeding 50 – 66 %; there remained 33 – 50 % of air deemed to form bubbles too small to be
709 discernible with the magnification of 160 times (Carte, 1961).

710 The present study suggests that the remaining solute is likely to be found in not only the puddles
711 of the highly concentrated solution but also, the veins or grain boundary grooves threading the
712 crystals. The problem of the varying behaviour of the surface brine puddles and brine in the ice grain
713 grooves should be examined. The difference in the dynamics of these two environments (Figure 6)
714 suggests the possibility of physically and/or chemically distinct behaviors; however, detailed research
715 in the given respect is yet to be conducted.

716

4.2 Relevance to impurity locations anticipated in previous laboratory experiments

718 The observed strong dependence of the ice microstructure on the freezing method suggests that
719 inferring the locations of impurities exclusively from the way the sample was prepared is not
720 straightforward; subtle details, such as the particular sample geometry and material properties of its
721 cover, may play a significant role. Although we found satisfactory reproducibility of the freezing
722 methods, variability was noticed within our research and other investigations in cases when the
723 freezing rates had not been precisely controlled (Malley et al., 2018). Certain variance of values should
724 always be supposed, even when the cooling protocol is kept unaltered as the freezing remains
725 stochastic (Vetráková et al., 2017;Krausková et al., 2016;Heger et al., 2006;Heger and Klan, 2007).
726 Importantly, a generalizable conclusion can be drawn from our current observations: for instances
727 where the freezing occurs from the surface inwards, the impurities are to be expected inside the ice
728 matrix, whereas when the process starts from the cooled pad, brine expulsion to the ice surface is
729 likely to materialize. This justified and expectable result should be applied to review the experiments
730 in which the impurities' locations were inferred merely based on the freezing procedure.

731 Thus, we can also assume, based on current and previous observations (Krausko et al.,
732 2014;Blackford et al., 2007), that the impurities will be contained primarily inside ice spheres prepared
733 by solution nebulization into LN. Experimental procedures essentially identical with our method for
734 the preparation of ice spheres were described by Kurkova et al. (2011); however, these authors
735 proposed that the impurities prevail on the outer surfaces of the ice spheres in the ice-air interface.
736 The difference between the present study and the approach adopted by Kurkova et al. lies in that salt
737 solutions are used in our case, whereas Kurkova et al. applied dilute organic compound solutions (with
738 $CuCl_2$ in some instances). We acknowledge that utilizing inorganic salts as a proxy for organic
739 compounds is only partly descriptive, but we assume that the compounds, inorganic or organic,
740 experience similar positions. All our numerous attempts to visualize low concentrations of organic
741 compounds ended unsuccessfully as we had not observed significant differences from frozen pure
742 water (data not shown).

743 In the present paper, we propose evidence for structural differences between the surface
744 (Figure 2-7) and the interior of the investigated ice samples (Figure 9). Certainly, after cutting the ice,
745 some amount of impurities will surface; however, our current observations indicate that most of the

21

The Cryosphere
Discussions

Open Access

EGU

746 compounds still remain inside the ice interior. No flowing out of the brine lamellae was observed at
747 −25 °C, even though the sample had slowly sublimed. Therefore, it seems unlikely that, by crushing the
748 original ice cubes, the organic impurities from the interior of the ice matrix could ascend to the ice-air
749 interface in an appreciable quantity, as was suggested by Kahan et al. (Kahan et al., 2010); such a
750 process would probably not occur unless the sample were exposed to increased temperatures for a
751 prolonged time or strong sublimation. In our opinion, the faster disappearance of the anthracene
752 fluorescence signal in crushed ice as compared to ice cubes might rather be explained by specific
753 optical properties of crushed ice (McFall and Anastasio, 2016).

754

5   Conclusion
756 We documented high sensitivity of the brine-ice topology towards freezing procedures. The
757 experimental setup of our ESEM allowed us to image the brine puddles together with ice grain grooves
758 and free ice surfaces for a wide range of CsCl concentrations and various freezing methods previously
759 applied in the laboratory examination of ice. The ice grain sizes and amount of the brine on the ice
760 surface were found to be determined by not only the initial solution concentration but, crucially, also
761 the freezing method and the thermal history of the sample. The freezing method also influenced the
762 sizes and distribution of the air bubbles, which tend to co-locate with the brine. Therefore, the
763 thermodynamic state of the sample (the temperature and impurities' concentrations) is not the sole
764 factor to determine the shape of the frozen water: the freezing rate and directionality play a critical
765 role in the brine distribution and will thus influence the transport properties within sea ice, including
766 the thermal conductivity and permeability. The presented micrographs clarified the possible porosity
767 and pore microstructure of sea ice. Strong hysteresis resulting in the brine accumulating on the ice
768 surface was found during the warming-cooling cycle. From the ice crystal sizes we infer the actual
769 freezing rates; the highest and lowest ones were found for the 16 °C supercooled solution and the
770 seeded sample at -2 °C, respectively. The interior of the in-capsule, LN-frozen ice samples exhibited
771 regularly spaced layers of ice and brine and did not reconstruct during the observation. Besides the
772 static snapshots, we were able to document the ice sublimation and recrystallization dynamics. During
773 the latter, the surface humps retarded the ice grain boundary migration. The recognition of the
774 impurities' locations within frozen samples should help to reinterpret previous assumptions and to
775 rationalize the observed behavior for laboratory experiments, all with the goal to describe the complex
776 interactions in natural ice. The obtained knowledge can also serve as an input for physical and chemical
777 models.

778

779 **Author contribution:** ĽV conducted the experiments and worked on the manuscript, JR and VN
780 conducted the experiments and constructed the microscope, DH proposed the experiments and
781 contributed to the writing of the manuscript. All authors contributed to the discussions.

783 **Competing interests:** The authors declare that they have no conflict of interest.

784

785

786

787

788 References:

789

790 Adda-Bedia, M., Kumar, S., Lechenault, F., Moulinet, S., Schillaci, M., and Vella, D.: Inverse Leidenfrost
791 Effect: Levitating Drops on Liquid Nitrogen, Langmuir, 32, 4179-4188, 10.1021/acs.langmuir.6b00574,
792 2016.
793 Anderson, D. L., and Weeks, W. F.: A theoretical analysis of sea-ice strength, Eos, Transactions
794 American Geophysical Union, 39, 632-640, 10.1029/TR039i004p00632, 1958.
795 Barnes, P. R. F., Mulvaney, R., Wolff, E. W., and Robinson, K.: A technique for the examination of polar
796 ice using the scanning electron microscope, Journal of Microscopy-Oxford, 205, 118-124,
797 10.1046/j.0022-2720.2001.00981.x, 2002.
798 Barnes, P. R. F., Wolff, E. W., Mallard, D. C., and Mader, H. M.: SEM studies of the morphology and
799 chemistry of polar ice, Microscopy Research and Technique, 62, 62-69, 10.1002/jemt.10385, 2003.
800 Bartels-Rausch, T., Jacobi, H. W., Kahan, T. F., Thomas, J. L., Thomson, E. S., Abbatt, J. P. D., Ammann,
801 M., Blackford, J. R., Bluhm, H., Boxe, C., Domine, F., Frey, M. M., Gladich, I., Guzmán, M. I., Heger, D.,
802 Huthwelker, T., Klán, P., Kuhs, W. F., Kuo, M. H., Maus, S., Moussa, S. G., McNeill, V. F., Newberg, J. T.,
803 Pettersson, J. B. C., Roeselová, M., and Sodeau, J. R.: A review of air–ice chemical and physical
804 interactions (AICI): liquids, quasi-liquids, and solids in snow, Atmos. Chem. Phys., 14, 1587-1633,
805 10.5194/acp-14-1587-2014, 2014.
806 Beine, H., Anastasio, C., Domine, F., Douglas, T., Barret, M., France, J., King, M., Hall, S., and Ullmann,
807 K.: Soluble chromophores in marine snow, seawater, sea ice and frost flowers near Barrow, Alaska,
808 Journal of Geophysical Research, 117, 10.1029/2011jd016650, 2012.
809 Blackford, J. R.: Sintering and microstructure of ice: a review, J. Phys. D Appl. Phys., 40, R355-R385,
810 10.1088/0022-3727/40/21/r02, 2007.
811 Blackford, J. R., Jeffree, C. E., Noake, D. F. J., and Marmo, B. A.: Microstructural evolution in sintered
812 ice particles containing NaCl observed by low-temperature scanning electron microscope, Proceedings
813 of the Institution of Mechanical Engineers, Part L: Journal of Materials: Design and Applications, 221,
814 151-156, 10.1243/14644207jmda134, 2007.
815 Bogdan, A., Molina, M. J., Tenhu, H., Bertel, E., Bogdan, N., and Loerting, T.: Visualization of Freezing
816 Process in situ upon Cooling and Warming of Aqueous Solutions, Scientific Reports, 4, 7414,
817 10.1038/srep07414, 2014.
818 Bogdan, A., and Molina, M. J.: Physical Chemistry of the Freezing Process of Atmospheric Aqueous
819 Drops, The Journal of Physical Chemistry A, 121, 3109-3116, 10.1021/acs.jpca.7b02571, 2017.
820 Bonner, O. D., and Cerutti, P. J.: The partial molar heat capacities of some solutes in water and
821 deuterium oxide, The Journal of Chemical Thermodynamics, 8, 105-112,
822 https://doi.org/10.1016/0021-9614(76)90082-3, 1976.
823 Brady, J. B.: MAGMA IN A BEAKER: ANALOG EXPERIMENTS WITH WATER AND VARIOUS SALTS OR
824 SUGAR FOR TEACHING IGNEOUS PETROLOGY, Canadian Mineralogist, 47, 457-471,
825 10.3749/canmin.47.2.457, 2009.
826 Braslavsky, I.: 15. Control of ice formation in biological samples, Cryobiology, 71, 168,
827 https://doi.org/10.1016/j.cryobiol.2015.05.021, 2015.
828 Cao, E., Chen, Y., Cui, Z., and Foster, P. R.: Effect of freezing and thawing rates on denaturation of
829 proteins in aqueous solutions, Biotechnology and Bioengineering, 82, 684-690, 10.1002/bit.10612,
830 2003.
831 Carte, A. E.: AIR BUBBLES IN ICE, Proceedings of the Physical Society of London, 77, 757-&,
832 10.1088/0370-1328/77/3/327, 1961.
833 Cohen-Adad, R.: Caesium Chloride, in: Alkali Metal and Ammonium Chlorides in Water and Heavy
834 Water (Binary Systems), Pergamon, Amsterdam, 375-412, 1991.
835 Cullen, D., and Baker, I.: Observation of impurities in ice, Microsc. Res.Techniq., 55, 198-207,
836 10.1002/jemt.10000, 2001.
837 Danilatos, G. D.: Introduction to the ESEM Instrument Microscopy Research and Technique, 25, 354-
838 361, 10.1002/jemt.1070250503, 1993.

839   Dash, J. G., Rempel, A. W., and Wettlaufer, J. S.: The physics of premelted ice and its geophysical
840   consequences, Reviews of Modern Physics, 78, 695-741, 10.1103/RevModPhys.78.695, 2006.
841   Domine, F., Bock, J., Voisin, D., and Donaldson, D. J.: Can We Model Snow Photochemistry? Problems
842   with the Current Approaches, J. Phys. Chem. A, 117, 4733-4749, 10.1021/jp3123314, 2013.
843   Dong, J. P., Hubel, A., Bischof, J. C., and Aksan, A.: Freezing-Induced Phase Separation and Spatial
844   Microheterogeneity in Protein Solutions, J. Phys. Chem. B, 113, 10081-10087, 10.1021/jp809710d,
845   2009.
846   Douglas, T. A., Domine, F., Barret, M., Anastasio, C., Beine, H. J., Bottenheim, J., Grannas, A., Houdier,
847   S., Netcheva, S., Rowland, G., Staebler, R., and Steffen, A.: Frost flowers growing in the Arctic ocean-
848   atmosphere–sea ice–snow interface: 1. Chemical composition, Journal of Geophysical Research, 117,
849   10.1029/2011jd016460, 2012.
850   Dubois, M., Royer, J. J., Weisbrod, A., and Shtuka, A.: Recostruction of Low-temperature Binary Phase
851   Diagrams Using a Constrained Least Squares Method - Application to the H2O CsCl System, European
852   Journal of Mineralogy, 5, 1145-1152, 1993.
853   Eichler, J., Kleitz, I., Bayer-Giraldi, M., Jansen, D., Kipfstuhl, S., Shigeyama, W., Weikusat, C., and
854   Weikusat, I.: Location and distribution of micro-inclusions in the EDML and NEEM ice cores using
855   optical microscopy and in situ Raman spectroscopy, The Cryosphere, 11, 1075-1090, 10.5194/tc-11-
856   1075-2017, 2017.
857   Fujiwara, S., and Nishimoto, Y.: Nonbiological Complete Differentiation of the Enantiomeric Isomers of
858   Amino Acids and Sugars by the Complexes of Gases with the Eutectic Compounds of Alkali Chlorides
859   and Water, Analytical Sciences, 14, 507-514, 10.2116/analsci.14.507, 1998.
860   Gao, D., Li, D., and Li, W.: Solubility of RbCl and CsCl in pure water at subzero temperatures, heat
861   capacity of RbCl(aq) and CsCl(aq) at T = 298.15 K, and thermodynamic modeling of RbCl + H 2 O and
862   CsCl + H 2 O systems, The Journal of Chemical Thermodynamics, 104, 201-211,
863   10.1016/j.jct.2016.09.031, 2017.
864   Gleick, P. H.: Water in Crisis. A Guide to the World's Fresh Water Resources, Oxford University Press,
865   1993.
866   Goldsack, D. E., and Franchetto, R.: Viscosity of Concentrated Electrolyte Solutions. 1. Concentration
867   Dependence at Fixed Temperature Can. J. Chem.-Rev. Can. Chim., 55, 1062-1072, 10.1139/v77-148,
868   1977.
869   Harrison, J. D.: Measurement of Brine Droplet Migration in Ice J. Appl. Phys., 36, 3811-&,
870   10.1063/1.1713953, 1965.
871   Heger, D., Jirkovsky, J., and Klan, P.: Aggregation of methylene blue in frozen aqueous solutions studied
872   by absorption spectroscopy, J. Phys. Chem. A, 109, 6702-6709, 10.1021/jp050439j, 2005.
873   Heger, D., Klanova, J., and Klan, P.: Enhanced protonation of cresol red in acidic aqueous solutions
874   caused by freezing, J. Phys. Chem. B, 110, 1277-1287, 10.1021/jp0553683, 2006.
875   Heger, D., and Klan, P.: Interactions of organic molecules at grain boundaries in ice: A solvatochromic
876   analysis, J. Photochem. Photobiol. A-Chem., 187, 275-284, 10.1016/j.jphotochem.2006.10.012, 2007.
877   Heger, D., Nachtigallova, D., Surman, F., Krausko, J., Magyarova, B., Brumovsky, M., Rubes, M., Gladich,
878   I., and Klan, P.: Self-Organization of 1-Methylnaphthalene on the Surface of Artificial Snow Grains: A
879   Combined Experimental-Computational Approach, J. Phys. Chem. A, 115, 11412-11422,
880   10.1021/jp205627a, 2011.
881   Hobbs, P. V.: Ice Physics, OUP Oxford, 2010.
882   Hullar, T., and Anastasio, C.: Direct visualization of solute locations in laboratory ice samples, The
883   Cryosphere, 10, 2057-2068, 10.5194/tc-10-2057-2016, 2016.
884   Hullar, T., Magadia, D., and Anastasio, C.: Photodegradation Rate Constants for Anthracene and Pyrene
885   Are Similar in/on Ice and in Aqueous Solution, Environ. Sci. Technol., 10.1021/acs.est.8b02350, 2018.
886   Chen, N. J., Morikawa, J., Kishi, A., and Hashimoto, T.: Thermal diffusivity of eutectic of alkali chloride
887   and ice in the freezing–thawing process by temperature wave analysis, Thermochim. Acta, 429, 73-79,
888   10.1016/j.tca.2004.11.010, 2005.
889   Chen, S., and Baker, I.: Observations of the morphology and sublimation-induced changes in uncoated
890   snow using scanning electron microscopy, Hydrol. Process., 24, 2041-2044, 10.1002/hyp.7689, 2010.

891   Chen, X., Shu, J., and Chen, Q.: Abnormal gas-liquid-solid phase transition behaviour of water observed
892   with in situ environmental SEM, Scientific Reports, 7, 46680, 10.1038/srep46680, 2017.
893   Cheng, J., Soetjipto, C., Hoffmann, M. R., and Colussi, A. J.: Confocal Fluorescence Microscopy of the
894   Morphology and Composition of Interstitial Fluids in Freezing Electrolyte Solutions, Journal of Physical
895   Chemistry Letters, 1, 374-378, 10.1021/jz9000888, 2010.
896   Jameel, F.: Formulation and process development strategies for manufacturing biopharmaceuticals.
897   Hershenson, S. (Ed.), John Wiley & Sons, 2010.
898   Kahan, T. F., Zhao, R., Jumaa, K. B., and Donaldson, D. J.: Anthracene Photolysis in Aqueous Solution
899   and Ice: Photon Flux Dependence and Comparison of Kinetics in Bulk Ice and at the Air-Ice Interface,
900   Environ. Sci. Technol., 44, 1302-1306, 10.1021/es9031612, 2010.
901   Kania, R., Malongwe, J. K. E., Nachtigallová, D., Krausko, J., Gladich, I., Roeselová, M., Heger, D., and
902   Klán, P.: Spectroscopic Properties of Benzene at the Air–Ice Interface: A Combined Experimental–
903   Computational Approach, The Journal of Physical Chemistry A, 118, 7535-7547, 10.1021/jp501094n,
904   2014.
905   Kasper, J. C., and Friess, W.: The freezing step in lyophilization: Physico-chemical fundamentals,
906   freezing methods and consequences on process performance and quality attributes of
907   biopharmaceuticals, European Journal of Pharmaceutics and Biopharmaceutics, 78, 248-263,
908   10.1016/j.ejpb.2011.03.010, 2011.
909   Ketcham, W. M., and Hobbs, P. V.: Step Growth on Ice During Freezing of Pure Water, Philosophical
910   Magazine, 18, 659-&, 10.1080/14786436808227468, 1968.
911   Klanova, J., Klan, P., Heger, D., and Holoubek, I.: Comparison of the effects of UV, H2O2/UV and
912   gamma- irradiation processes on frozen and liquid water solutions of monochlorophenols,
913   Photochemical & Photobiological Sciences, 2, 1023-1031, 10.1039/b303483f, 2003.
914   Knipping, E. M., Lakin, M. J., Foster, K. L., Jungwirth, P., Tobias, D. J., Gerber, R. B., Dabdub, D., and
915   Finlayson-Pitts, B. J.: Experiments and Simulations of Ion-Enhanced Interfacial Chemistry on Aqueous
916   NaCl Aerosols, Science, 288, 301-306, 10.1126/science.288.5464.301, 2000.
917   Krausko, J., Runštuk, J., Neděla, V., Klán, P., and Heger, D.: Observation of a Brine Layer on an Ice
918   Surface with an Environmental Scanning Electron Microscope at Higher Pressures and Temperatures,
919   Langmuir, 30, 5441-5447, 10.1021/la500334e, 2014.
920   Krausko, J., Malongwe, J. K. E., Bičanová, G., Klán, P., Nachtigallová, D., and Heger, D.: Spectroscopic
921   Properties of Naphthalene on the Surface of Ice Grains Revisited: A Combined Experimental–
922   Computational   Approach,   The   Journal   of   Physical   Chemistry   A,   119,   8565-8578,
923   10.1021/acs.jpca.5b00941, 2015a.
924   Krausko, J., Ondrušková, G., and Heger, D.: Comment on "Photolysis of Polycyclic Aromatic
925   Hydrocarbons on Water and Ice Surfaces" and on "Nonchromophoric Organic Matter Suppresses
926   Polycyclic Aromatic Hydrocarbon Photolysis in Ice and at Ice Surfaces", The Journal of Physical
927   Chemistry A, 119, 10761-10763, 10.1021/acs.jpca.5b08276, 2015b.
928   Krausková, Ľ., Procházková, J., Klašková, M., Filipová, L., Chaloupková, R., Malý, S., Damborský, J., and
929   Heger, D.: Suppression of protein inactivation during freezing by minimizing pH changes using ionic
930   cryoprotectants, International Journal of Pharmaceutics, 509, 41-49, 10.1016/j.ijpharm.2016.05.031,
931   2016.
932   Kurkova, R., Ray, D., Nachtigallova, D., and Klan, P.: Chemistry of Small Organic Molecules on Snow
933   Grains: The Applicability of Artificial Snow for Environmental Studies, Environ. Sci. Technol., 45, 3430-
934   3436, 10.1021/es104095g, 2011.
935   Labadia, C. F., and Buttle, J. M.: Road salt accumulation in highway snow banks and transport through
936   the unsaturated zone of the Oak Ridges Moraine, southern Ontario, Hydrol. Process., 10, 1575-1589,
937   10.1002/(sici)1099-1085(199612)10:12<1575::aid-hyp502>3.0.co;2-1, 1996.
938   Lake, R. A., and Lewis, E. L.: Salt rejection by sea ice during growth, Journal of Geophysical Research,
939   75, 583-597, 10.1029/JC075i003p00583, 1970.
940   Light, B., Brandt, R. E., and Warren, S. G.: Hydrohalite in cold sea ice: Laboratory observations of single
941   crystals, surface accumulations, and migration rates under a temperature gradient, with application to
942   "Snowball Earth", Journal of Geophysical Research, 114, 10.1029/2008jc005211, 2009.

The Cryosphere

Discussions

Open Access

EGU

943   Losert, W., Shi, B. Q., and Cummins, H. Z.: Evolution of dendritic patterns during alloy solidification:
944   Onset of the initial instability, Proceedings of the National Academy of Sciences, 95, 431-438,
945   10.1073/pnas.95.2.431, 1998.
946   Macklin, W. C., and Ryan, B. F.: Habits of Ice Grown in Supercooled Water and Aqueous Solutions
947   Philosophical Magazine, 14, 847-&, 10.1080/14786436608211977, 1966.
948   Maeda, N., Israelachvili, J. N., and Kohonen, M. M.: Evaporation and instabilities of microscopic
949   capillary bridges, Proceedings of the National Academy of Sciences, 100, 803-808,
950   10.1073/pnas.0234283100, 2003.
951   Magee, N. B., Miller, A., Amaral, M., and Cumiskey, A.: Mesoscopic surface roughness of ice crystals
952   pervasive across a wide range of ice crystal conditions, Atmospheric Chemistry and Physics, 14, 12357-
953   12371, 10.5194/acp-14-12357-2014, 2014.
954   Malley, P. P. A., Chakraborty, S., and Kahan, T. F.: Physical Characterization of Frozen Saltwater
955   Solutions   Using   Raman   Microscopy,   ACS   Earth   and   Space   Chemistry,
956   10.1021/acsearthspacechem.8b00045, 2018.
957   Massom, R. A., Eicken, H., Hass, C., Jeffries, M. O., Drinkwater, M. R., Sturm, M., Worby, A. P., Wu, X.,
958   Lytle, V. I., Ushio, S., Morris, K., Reid, P. A., Warren, S. G., and Allison, I.: Snow on Antarctic sea ice, Rev.
959   Geophys., 39, 413-445, 10.1029/2000rg000085, 2001.
960   Maus, S.: Prediction of the cellular microstructure of sea ice by morphological stability theory, Physics
961   and Chemistry of Ice, edited by: Kuhs, W. F., 371-382 pp., 2007.
962   McCarthy, C., Blackford, J. R., and Jeffree, C. E.: Low-temperature-SEM study of dihedral angles in the
963   ice-I/sulfuric acid partially molten system, Journal of Microscopy, 249, 150-157, 10.1111/jmi.12003,
964   2013.
965   McFall, A. S., and Anastasio, C.: Photon flux dependence on solute environment in water ices,
966   Environmental Chemistry, 13, 682, 10.1071/en15199, 2016.
967   Monnin, C., and Dubois, M.: Thermodynamics of the CsCl-H2O system at low temperatures, European
968   Journal of Mineralogy, 11, 477-482, 1999.
969   Nagashima, K., and Furukawa, Y.: Solute Distribution in front of an Ice/Water Interface during
970   Directional Growth of Ice Crystals and Its Relationship to Interfacial Patterns, The Journal of Physical
971   Chemistry B, 101, 6174-6176, 10.1021/jp963172k, 1997.
972   Nair, M., Husmann, A., Cameron, R. E., and Best, S. M.: In situ

973   ESEM imaging of the vapor-pressure-dependent sublimation-induced morphology of ice, Physical
974   Review Materials, 2, 10.1103/PhysRevMaterials.2.040401, 2018.
975   Nakai, T., Sawamura, S., and Taniguchi, Y.: EFFECT OF PRESSURE ON THE VISCOSITY OF AQUEOUS
976   CESIUM-CHLORIDE SOLUTION AT 25-DEGREES-C, Journal of Molecular Liquids, 65-6, 365-368,
977   10.1016/0167-7322(95)00832-4, 1995.
978   Nedela, V.: Methods for additive hydration allowing observation of fully hydrated state of wet samples
979   in environmental SEM, Microscopy Research and Technique, 70, 95-100, 10.1002/jemt.20390, 2007.
980   Nedela, V., Tihlarikova, E., Runstuk, J., and Hudec, J.: High-efficiency detector of secondary and
981   backscattered electrons for low-dose imaging in the ESEM, Ultramicroscopy, 184, 1-11,
982   10.1016/j.ultramic.2017.08.003, 2018.
983   Nedĕla, V., Konvalina, I., Oral, M., and Hudec, J.: The Simulation of Energy Distribution of Electrons
984   Detected by Segmental Ionization Detector in High Pressure Conditions of ESEM, Microscopy and
985   Microanalysis, 21, 264-269, 10.1017/S1431927615013483, 2015.
986   Notz, D., and Worster, M. G.: Desalination processes of sea ice revisited, Journal of Geophysical
987   Research, 114, 10.1029/2008jc004885, 2009.
988   Nye, J. F.: The rotting of temperate ice, J. Cryst. Growth, 113, 465-476, https://doi.org/10.1016/0022-
989   0248(91)90081-F, 1991.
990   Ohno, H., Igarashi, M., and Hondoh, T.: Salt inclusions in polar ice core: Location and chemical form of
991   water-soluble   impurities,   Earth   and   Planetary   Science   Letters,   232,   171-178,
992   10.1016/j.epsl.2005.01.001, 2005.

993   Ohno, H., Igarashi, M., and Hondoh, T.: Characteristics of salt inclusions in polar ice from Dome Fuji,
994   East Antarctica, Geophys. Res. Lett., 33, 10.1029/2006gl025774, 2006.
995   Ondrušková, G., Krausko, J., Stern, J. N., Hauptmann, A., Loerting, T., and Heger, D.: Distinct Speciation
996   of Naphthalene Vapor Deposited on Ice Surfaces at 253 or 77 K: Formation of Submicrometer-Sized
997   Crystals or an Amorphous Layer, The Journal of Physical Chemistry C, 122, 11945-11953,
998   10.1021/acs.jpcc.8b03972, 2018.
999   Petrenko, V. F., and Whitworth, R. W.: Physics of ice, Oxford University Press, Oxford, 1999.
1000 Pinzer, B. R., and Schneebeli, M.: Snow metamorphism under alternating temperature gradients:
1001 Morphology and recrystallization in surface snow, Geophys. Res. Lett., 36, 4, 10.1029/2009gl039618,
1002 2009.
1003 Ram, K., and Anastasio, C.: Photochemistry of phenanthrene, pyrene, and fluoranthene in ice and
1004 snow, Atmos. Environ., 43, 2252-2259, 10.1016/j.atmosenv.2009.01.044, 2009.
1005 Reiser, S., Horsch, M., and Hasse, H.: Temperature Dependence of the Density of Aqueous Alkali Halide
1006 Salt Solutions by Experiment and Molecular Simulation, Journal of Chemical & Engineering Data, 59,
1007 3434-3448, 10.1021/je500420g, 2014.
1008 Roessl, U., Leitgeb, S., and Nidetzky, B.: Protein freeze concentration and micro-segregation analysed
1009 in a temperature-controlled freeze container, Biotechnology Reports, 6, 108-111,
1010 10.1016/j.btre.2015.03.004, 2015.
1011 Rohatgi, P. K., and Adams, C. M.: Ice–Brine Dendritic Aggregate formed on Freezing of Aqueous
1012 Solutions, J. Glaciol., 6, 663-679, Doi: 10.1017/s0022143000019936, 1967.
1013 Rohatgi, P. K., Jain, S. M., and Adams, C. M.: Effect of Magnetic and Electrical Fields on Dendritic
1014 Freezing of Aqeous Sulutions of Sodium Chloride Materials Science and Engineering, 15, 283-290,
1015 10.1016/0025-5416(74)90062-7, 1974.
1016 Rosenthal, W., Saleta, J., and Dozier, J.: Scanning electron microscopy of impurity structures in snow,
1017 Cold Regions Science and Technology, 47, 80-89, 10.1016/j.coldregions.2006.08.006, 2007.
1018 Salnikova, M., Varshney, D., and Shalaev, E.: Heterogeneity of Protein Environments in Frozen
1019 Solutions and in the Dried State, 11-24, 10.1007/978-1-4939-2383-0_2, 2015.
1020 Steinbach, F., Kuiper, E.-J. N., Eichler, J., Bons, P. D., Drury, M. R., Griera, A., Pennock, G. M., and
1021 Weikusat, I.: The Relevance of Grain Dissection for Grain Size Reduction in Polar Ice: Insights from
1022 Numerical Models and Ice Core Microstructure Analysis, Frontiers in Earth Science, 5,
1023 10.3389/feart.2017.00066, 2017.
1024 Suzuki, S., Nakajima, A., Yoshida, N., Sakai, M., Hashimoto, A., Kameshima, Y., and Okada, K.: Freezing
1025 of water droplets on silicon surfaces coated with various silanes, Chem. Phys. Lett., 445, 37-41,
1026 10.1016/j.cplett.2007.07.066, 2007.
1027 Thomas, D. N.: Sea Ice, Wiley-Blackwell, Chichester, UK, 2017.
1028 Tihlarikova, E., Nedela, V., and Shiojiri, M.: In situ study of live specimens in an environmental scanning
1029 electron microscope, Microsc Microanal, 19, 914-918, 10.1017/S1431927613000603, 2013.
1030 Tokumasu, K., Harada, M., and Okada, T.: X-ray Fluorescence Imaging of Frozen Aqueous NaCl
1031 Solutions, Langmuir, 32, 527-533, 10.1021/acs.langmuir.5b04411, 2016.
1032 Trivedi, R., and Kurz, W.: Solidification microstructures: A conceptual approach, Acta Metallurgica et
1033 Materialia, 42, 15-23, https://doi.org/10.1016/0956-7151(94)90044-2, 1994.
1034 Vega, C. P., Isaksson, E., Schlosser, E., Divine, D., Martma, T., Mulvaney, R., Eichler, A., and
1035 Schwikowski-Gigar, M.: Variability of sea salts in ice and firn cores from Fimbul Ice Shelf, Dronning
1036 Maud Land, Antarctica, The Cryosphere, 12, 1681-1697, 10.5194/tc-12-1681-2018, 2018.
1037 Vetráková, Ľ., Vykoukal, V., and Heger, D.: Comparing the acidities of aqueous, frozen, and freeze-dried
1038 phosphate buffers: Is there a "pH memory" effect?, International Journal of Pharmaceutics, 530, 316-
1039 325, 10.1016/j.ijpharm.2017.08.005, 2017.
1040 Wåhlin, J., Leisinger, S., and Klein-Paste, A.: The effect of sodium chloride solution on the hardness of
1041 compacted snow, Cold Regions Science and Technology, 102, 1-7, 10.1016/j.coldregions.2014.02.002,
1042 2014.
1043 Weeks, W. F.: On Sea Ice, On Sea Ice, 1-665 pp., 2010.

1044   Wettlaufer, J. S., Worster, M. G., and Huppert, H. E.: Natural convection during solidification of an alloy
1045   from above with application to the evolution of sea ice, Journal of Fluid Mechanics, 344, 291-316,
1046   10.1017/s0022112097006022, 1997.
1047   Wilson, P. W., and Haymet, A. D. J.: Workman-Reynolds freezing potential measurements between ice
1048   and dilute salt solutions for single ice crystal faces, J. Phys. Chem. B, 112, 11750-11755, 2008.
1049   Yan, F., Xiong, W., and Faierson, E.: Grain Structure Control of Additively Manufactured Metallic
1050   Materials, Materials, 10, 1260, 10.3390/ma10111260, 2017.
1051   Yang, X., Neděla, V., Runštuk, J., Ondrušková, G., Krausko, J., Vetráková, Ľ., and Heger, D.: Evaporating
1052   brine from frost flowers with electron microscopy and implications for atmospheric chemistry and sea-
1053   salt aerosol formation, Atmos. Chem. Phys., 17, 6291-6303, 10.5194/acp-17-6291-2017, 2017.
1054   Zobrist, B., Marcolli, C., Pedernera, D. A., and Koop, T.: Do atmospheric aerosols form glasses?,
1055   Atmospheric Chemistry and Physics, 8, 5221-5244, 10.5194/acp-8-5221-2008, 2008.

1056